Physics of Fluids ARTICLE scitation.org/journal/phf

Impact of bulk viscosity on flow morphology of shock-accelerated cylindrical light bubble in diatomic and polyatomic gases

Cite as: Phys. Fluids 33, 066103 (2021); doi: 10.1063/5.0051169
Submitted: 23 March 2021 · Accepted: 19 May 2021 ·
Published Online: 9 June 2021

Satyvir Singh,[1,a)] Marco Battiato,[1] and R. S. Myong[2]

AFFILIATIONS

[1]School of Physical and Mathematical Sciences, Nanyang Technological University, 21 Nanyang Link, Singapore 637371
[2]School of Mechanical and Aerospace Engineering and ACTRC, Gyeongsang National University, Jinju, Gyeongnam 52828, South Korea

[a)]Author to whom correspondence should be addressed: satyvir.singh@ntu.edu.sg

ABSTRACT

Shock-accelerated bubbles have long been an intriguing topic for understanding the fundamental physics of turbulence generation and mixing caused by the Richtmyer–Meshkov instability. In this study, the impact of bulk viscosity on the flow morphology of a shock-accelerated cylindrical light bubble in diatomic and polyatomic gases is investigated numerically. An explicit mixed-type modal discontinuous Galerkin scheme with uniform meshes is employed to solve a two-dimensional system of unsteady physical conservation laws derived rigorously from the Boltzmann–Curtiss kinetic equations. We also derive a new complete viscous compressible vorticity transport equation including the bulk viscosity. The numerical results show that, during the interaction between a planar shock wave and a cylindrical light bubble, the bulk viscosity associated with the viscous excess normal stress in diatomic and polyatomic gases plays an important role. The diatomic and polyatomic gases cause significant changes in flow morphology, resulting in complex wave patterns, vorticity generation, vortex formation, and bubble deformation. In contrast to monatomic gases, diatomic and polyatomic gases produce larger rolled-up vortex chains, various inward jet formations, and large mixing zones with strong, large-scale expansion. The effects of diatomic and polyatomic gases are explored in detail through phenomena such as the vorticity generation, degree of nonequilibrium, enstrophy, and dissipation rate. Furthermore, the evolution of the shock trajectories and interface features is investigated. Finally, the effects of bulk viscosity on the flow physics of shock-accelerated cylindrical light bubble are comprehensively analyzed.

I. INTRODUCTION

The Richtmyer–Meshkov (RM) instability[1,2] occurs when an incident shock (IS) wave accelerates an initially disruptive interface between two fluids of different gas properties. The incident shock wave and disruptive interface produce density and pressure gradients during the interaction process, which contribute to a misalignment between those gradients. Consequently, some specific flow structures emerge and intensify the gas mixing, eventually improving the turbulent mixing phenomena. The RM instability has received considerable attention in many natural and engineering fields and has applications in inertial confinement fusion,[3] supernova explosions,[4] medical shock wave lithotripsy,[5] scramjet combustion,[6,7] and astrophysics.[8]

In recent decades, shock-accelerated bubbles have been widely studied in an attempt to understand the physical configuration of the RM instability. The flow configuration in a shock-accelerated bubble is basically classified based on the Atwood number. If ρ_b and ρ_g are the densities of the unshocked bubble and its surrounding unshocked gas, respectively, the Atwood number can be defined as $A_t = (\rho_b - \rho_g)/(\rho_b + \rho_g)$. If the bubble gas is lighter than the ambient gas, the Atwood number becomes negative, that is, $A_t < 0$, resulting in a "heavy–light" or "divergent" configuration. In contrast, if the bubble gas is heavier than the ambient gas, the Atwood number becomes positive, that is, $A_t > 0$, and this case gives the "light–heavy" or "convergent" configuration. The typical flow configurations during the early stages of the shock-accelerated bubble process are depicted schematically in Fig. 1. The deformation of the bubble interface can be seen in the flow patterns of divergent [Fig. 1(a)] and convergent [Fig. 1(b)] configurations. After colliding with the incident shock wave, the region upstream of the bubble (the left side) starts to deform. The shock wave generated within a light bubble propagates faster than the

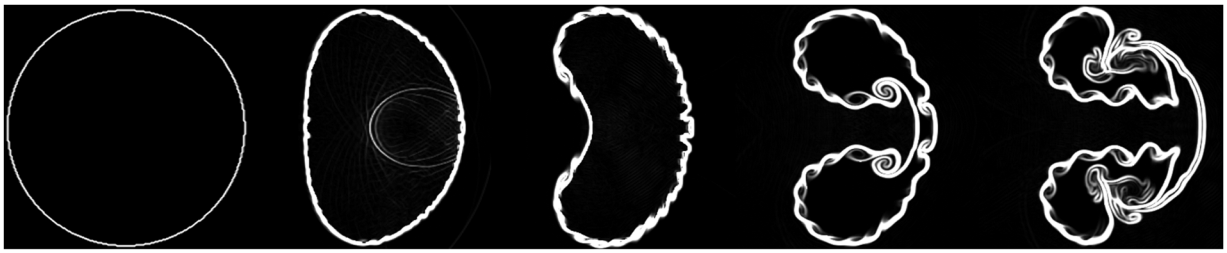

(a) Divergent configuration

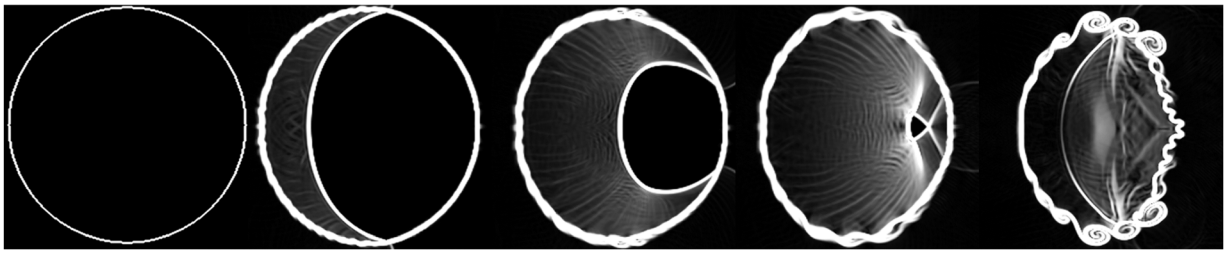

(b) Convergent configuration

FIG. 1. Deformation of a bubble interface during interaction process: (a) divergent configuration for $A_t < 0$, and (b) convergent configuration for $A_t > 0$.

incident shock wave outside the bubble. This is caused by a mismatch in the acoustic impedances of the flow constituents across the interface and results in the bubble deforming into a divergent configuration, as shown in Fig. 1(a). In the case of a heavy bubble, the transmitted shock wave propagates slower than the incident shock wave and may become focused at the downstream pole of the bubble and collapse into a single shock-focusing, high-pressure point. Consequently, the bubble deforms into a convergent configuration, as illustrated in Fig. 1(b).

As the incident shock wave strikes the bubble, the baroclinic effect creates a vorticity distribution on the interface between the bubble and its surroundings. The fundamental physics that occur during the interaction between the incident shock wave and the gas bubble can be interpreted using the equation of vorticity transport.[9,10] This equation, which includes several physically distinct quantities, can be defined as follows:

$$\frac{D\boldsymbol{\omega}}{Dt} = (\boldsymbol{\omega}\cdot\nabla)\mathbf{u} - \boldsymbol{\omega}(\nabla\cdot\mathbf{u}) + \frac{\mu}{\rho}\nabla^2\boldsymbol{\omega} + \frac{1}{\rho^2}(\nabla\rho\times\nabla p) - \frac{\mu}{\rho^2}(\nabla\rho\times\nabla^2\mathbf{u}) - \left(\frac{1}{3}+f_b\right)\frac{\mu}{\rho^2}\nabla\rho\times\nabla(\nabla\cdot\mathbf{u}), \quad (1)$$

where $\boldsymbol{\omega}(=\nabla\times\mathbf{u})$, ρ, $\mathbf{u}$, p, and μ represent the vorticity, density, velocity, pressure, and shear viscosity, respectively. We believe this equation is new (the last two terms on the right-hand side have been incorrectly omitted in the previous literature). The equation was derived under the assumption of constant transport coefficients. (The exact viscous vorticity transport equation with varying transport coefficients, but without Stokes' hypothesis, is summarized in detail in the Appendix.) The factor $f_b = \mu_b/\mu$ denotes the ratio of the bulk viscosity to the shear viscosity and will play an important role in the compressible shock and bubble interaction. Note the difference from the well-known incompressible vorticity transport equation first derived by Helmholtz (ν being the kinematic viscosity), that is,

$$\frac{D\boldsymbol{\omega}}{Dt} = (\boldsymbol{\omega}\cdot\nabla)\mathbf{u} + \nu\nabla^2\boldsymbol{\omega}.$$

On the right-hand side of Eq. (1), the term $\boldsymbol{\omega}(\nabla\cdot\mathbf{u})$ represents the fluid convection and thermal expansion, which is only appropriate for highly compressible fluids. The term $(\boldsymbol{\omega}\cdot\nabla)\mathbf{u}$ represents the vortex stretching, which is critical for three-dimensional turbulence and mixing. The term $(\mu/\rho)\nabla^2\boldsymbol{\omega}$ represents the acceleration due to the diffusion of vorticity. The term $(1/\rho^2)(\nabla\rho\times\nabla p)$ denotes the baroclinic vorticity, which is responsible for the production of small-scale rolled-up vortices at the bubble interface. Moreover, this term is most prominent at the top and bottom ends of a vertical bubble due to the extreme misalignment of the density and pressure gradients. The term $(\mu/\rho^2)(\nabla\rho\times\nabla^2\mathbf{u})$ represents the vorticity generated by the combination of density gradient and velocity diffusion. Finally, the last term $(1/3+f_b)(\mu/\rho^2)[\nabla\rho\times\nabla(\nabla\cdot\mathbf{u})]$ represents the vorticity generated by the combination of density and velocity divergence gradients of viscous origin, which resemble the baroclinic vorticity generated by the combination of density and pressure gradients. In addition, there exists a term directly related to the bulk viscosity, $f_b(\mu/\rho^2)[\nabla\rho\times\nabla(\nabla\cdot\mathbf{u})]$. As the factor $f_b = \mu_b/\mu$ is close to unity in the case of diatomic gases, it may play an important role in the compressive shock–bubble interaction in diatomic and polyatomic gases.

There have been tremendous efforts in the past to understand the flow morphology of shock-accelerated bubbles relevant to the RM instability through experiments, theoretical analysis, and computational simulations. The shock-accelerated bubble problem was first explored experimentally in the seminal works of Markstein[11] and Rudinger and Somers,[12] which explained a knotty turbulent flow field

phenomenon with long-lived vortex rings (VR). Haas and Sturtevant[13] experimentally studied the shock-accelerated bubble problem with lighter and heavier gas bubbles, and explored the wave patterns phenomenon for both convergent and divergent situations. Later, Jacobs[14,15] experimentally investigated the high-quality flow morphology of shock-accelerated bubbles based on planar laser-induced fluorescence technology. Layes *et al.*[16,17] experimentally explored the flow morphology of shock-accelerated bubbles with different gases via high-speed camera shadowgraph diagnostics. Moreover, Ranjan *et al.*[18,19] conducted experimental studies of the divergent-geometry-based flow morphology in shock-accelerated bubbles with the aid of planar laser diagnostics.

Numerous numerical and theoretical studies have also been conducted. Picone and Boris[55] and Quirk and Karni[20] performed comprehensive studies of the flow morphology of the shock–bubble interaction and reproduced the experimental results obtained by Haas and Sturtevant.[13] Further, Zabusky and Zeng[21] simulated the Euler equations for the flow morphology in the interaction of planar shocks with an R_{12} axisymmetric spherical bubble and observed that a weak jet was expelled due to the collapsing shock-bounded cavities in fast/slow spherical and near-spherical configurations. Later, the impact of the incident shock Mach number on the flow morphology of shock-accelerated bubbles was numerically examined by Bagabir and Drikakis,[22] who revealed additional gas dynamic features as the Mach number increased. Niederhaus *et al.*[23] performed numerical simulations of a multifluid Eulerian configuration to investigate the flow morphologies and integral properties of shock-accelerated bubbles, and explored the effects of different Atwood numbers and shock intensities. Zhu and his collaborators[24–26] numerically explored the flow morphology in the interaction between shock wave and gas bubble with light and heavy bubbles, and performed a detailed analysis of the shock-focusing phenomenon and the generation and evolution of vortex rings and jets. Rybakin and Goryachev[27]] investigated the deformation and instability of a low-density gas bubble, the formation and evolution of vortex rings, and the shock wave–bubble configuration. Later, Rybakin *et al.*[28–30] presented the three-dimensional numerical simulations for the interaction process of the supernova strong shock wave with interstellar molecular cloud and investigated the processes of deformation and fragmentation of molecular cloud in detail. The vortex breakdown behavior of the scaling criterion in shock-cylindrical bubble interaction was studied numerically and theoretically by Wang *et al.*,[31] who found that viscosity leads to vortex breakdown. Recently, Singh[32] numerically investigated the effects of the Atwood number on the flow morphology of a shock-accelerated square bubble containing different gases.

Intriguingly, the majority of existing theoretical and numerical research on the shock-accelerated bubble problem has explored the negligible thermal nonequilibrium effects, which are directly connected to the internal modes of diatomic and polyatomic gases—the rotational and vibrational modes. These studies have focused on the Euler or Navier–Stokes–Fourier (NSF) equations, which are derived from the Boltzmann kinetic equation with the assumption of thermal equilibrium and near-thermal equilibrium, respectively, and are considered to be the *de facto* mathematical models for any possible flow problem, including compressible gas flows.

Another vital assumption behind the NSF relations is the so-called Stokes hypothesis, introduced by Stokes[33] in 1845, which states that the bulk viscosity μ_b vanishes (λ and μ being the second coefficient of viscosity and the shear viscosity of the fluid, respectively), that is,

$$\mu_b \equiv \lambda + \frac{2}{3}\mu = 0, \quad \text{equivalently,} \quad \lambda = -\frac{2}{3}\mu. \tag{2}$$

While Stokes' hypothesis is believed to be valid in the case of monatomic gases such as argon, there is growing proof that this is not the case with diatomic and polyatomic gases such as nitrogen, methane, and carbon dioxide.[34–49]

Examples of such cases include the inner structure of strong shock waves in diatomic gases and hypersonic entry into the Mars atmosphere, which consists mostly of carbon dioxide. A recent experimental study on the second-mode instability in the laminar-to-turbulence transition in hypersonic boundary layers[40] showed that, for a real diatomic gas, the growth and decay of the second mode are accompanied by a dilatation process that leads to a 50% increase in dilatation dissipation in comparison with Stokes' hypothesis. Moreover, direct numerical simulations of turbulence by Pan and Johnsen[42] showed that the bulk viscosity increases the decay rate of the turbulent kinetic energy significantly, and dilatation is reduced by over two orders of magnitude within the first two eddy-turnover times. Further, Singh *et al.*[45] found a significant increase in enstrophy with increasing bulk viscosity, which is directly related to the rotational mode of a gas molecule. Later, Singh *et al.*[48] investigated the topology of the high-order constitutive model beyond the conventional NSF equations and Stokes' hypothesis. Recently, Singh and Battiato[49] numerically studied the behavior of a shock-accelerated cylindrical heavy bubble under the nonequilibrium conditions of diatomic and polyatomic gases.

Inspired by these developments, this study aims to investigate the impact of bulk viscosity on the flow morphology of shock-accelerated cylindrical light bubble based on the Boltzmann–Curtiss kinetic equation for diatomic and polyatomic gases. Emphasis is focused on the impacts of thermal nonequilibrium and the bulk viscosity associated with the viscous excess normal stress on diatomic and polyatomic gases, and their effects on the flow morphology of shock-accelerated cylindrical light bubble. *To the best of the authors' knowledge, there have been no reports in the literature on the impact of bulk viscosity on the flow morphology of shock-accelerated cylindrical light bubble in diatomic and polyatomic gases.* Furthermore, this work can be viewed as a complement to the RM instability research, investigating the effects of bulk viscosity on the dynamics of shock-accelerated cylindrical light bubble.

The remainder of this paper is organized as follows. In Sec. II, the problem setup is presented and we consider the Boltzmann–Curtiss kinetic equation for diatomic and polyatomic gases. The physical conversation laws are formulated, and the bulk viscosity is estimated based on kinetic and continuum theories. In Sec. III, the numerical scheme is introduced and validated, and grid refinement analysis is performed with precision estimation. In Sec. IV, the numerical results for shock-accelerated cylindrical light bubble in diatomic and polyatomic gases are discussed in detail. First, the overall flow morphology is visualized. Next, the effects of diatomic and polyatomic gases on shock-accelerated cylindrical light bubble are systematically analyzed to illustrate the differences in contrast to monatomic gases. Consequently, the effects of bulk viscosity are clarified. Finally, concluding remarks

outlining further developments along the lines of the present study are given in Sec. V.

II. PROBLEM SETUP AND COMPUTATIONAL MODEL

A. Problem setup

Figure 2 shows a schematic diagram of the flow model used to simulate an incident shock (IS) wave interacting with a cylindrical bubble surrounded with ambient gas. A rectangular domain of $[0, 220] \times [0, 90]$ is adopted for the numerical simulation of the shock-accelerated bubble problem, where a moving IS wave and a cylindrical stationary bubble are considered. The IS wave with Mach number M_s propagates from left to right with respect to the initial shock wave in the computational domain and interacts with the cylindrical bubble. The initial position of the shock wave is at $x = 30$ mm from the left-hand side of the computational domain. The bubble radius is taken as $R_b = 25$ mm, and the location of the center of the bubble is set as $(x_c, y_c) = (60, 45)$ mm. The initial pressure and temperature are set to $P_0 = 101,325$ Pa and $T_0 = 293$ K, respectively, around the gas bubble. As helium (He) gas has been widely adopted as a light gas in previous studies on the RM instability, we also consider He gas with a density of $\rho_g = 0.16\text{kg/m}^3$ inside the cylindrical bubble. For the ambient gas, three different gases are considered in this study—monatomic argon, diatomic nitrogen, and polyatomic methane. The left boundary is set to be the inflow, while the upper, bottom, and right boundaries are set to be outflow boundaries.

B. Physical conservation laws for diatomic and polyatomic gases

Shock-accelerated bubble problems are basically solved by simulating the compressible multispecies flow model with a gas mixture.[53,54] Interestingly, Picone and Boris,[55] Samtaney and Zabusky,[56] Quirk and Karni,[20] and Bagabir and Drikakis[22] have found that assigning different specific heat capacities γ to each gas does not affect the qualitative details of the vorticity generation, particularly the creation of large-scale structures. According to Quirk and Karni,[20] for the problem of a shock-accelerated bubble "…the errors introduced by the single-gas model assumption are not catastrophic and to some extent may be tolerated." However, such errors cannot be tolerated in applications such as air–fuel mixing in a supersonic combustion system, where temperature changes will substantially affect the mixing. Recently, Latini and Schilling[57] numerically investigated the growth dynamics of two- and three-dimensional single-mode reshocked air/SF_6 RM instabilities by considering a single specific heat ratio γ. Based on the above discussion, the present shock-accelerated cylindrical light bubble problem is configured as an unsteady compressible laminar flow that assumes a single-component perfect gas with a specific heat ratio of γ.

In the absence of an external force field, the well-known Boltzmann–Curtiss kinetic equation[58] for diatomic and (linear) polyatomic molecules with a moment of inertia I_m and an angular momentum $\mathbf{j}$ can be expressed as

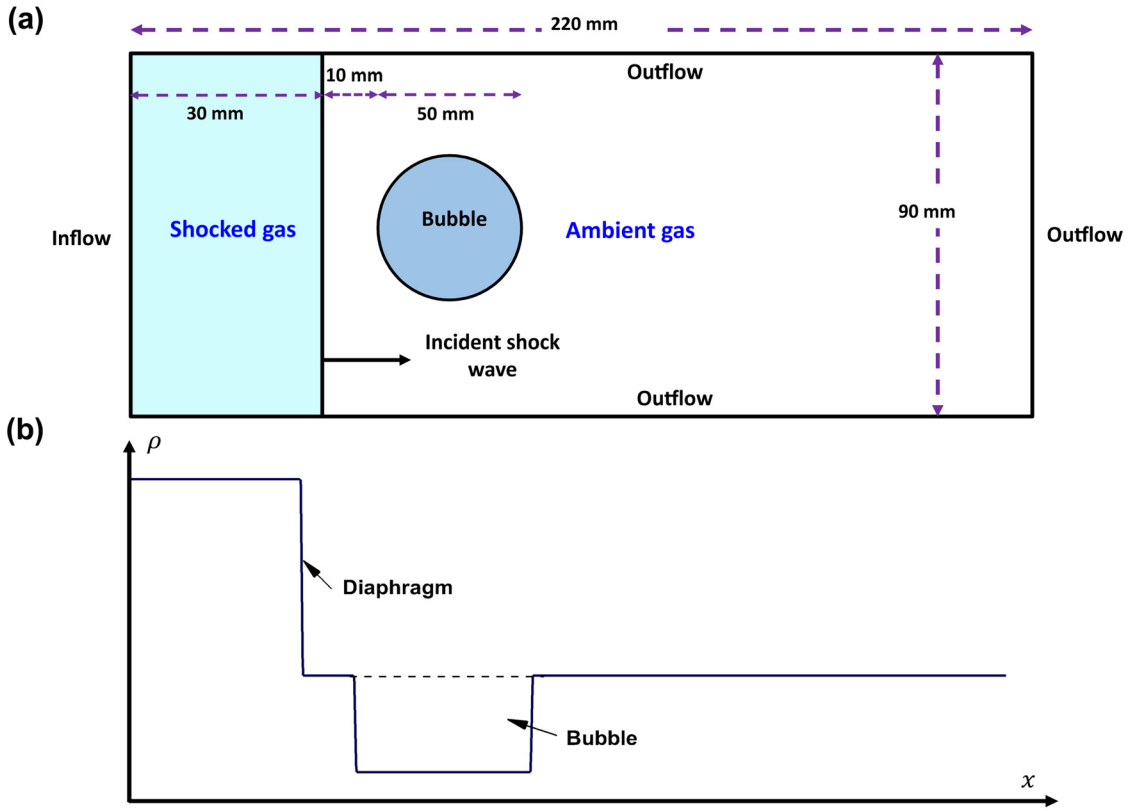

FIG. 2. Problem setup: schematic diagram for (a) computation setup, and (b) density distribution.

$$\left(\frac{\partial f}{\partial t}+\mathbf{v}\cdot\nabla+\frac{j}{I_m}\frac{\partial}{\partial\psi}\right)f(\mathbf{v},\mathbf{r},\mathbf{j},\psi,t)=R[f]. \tag{3}$$

Here, $f, \mathbf{v}, \mathbf{r}, \psi, j$, and $R[f]$ are defined as the density distribution function, particle velocity, particle position, azimuthal angle of the particle orientation, magnitude of the angular momentum vector $\mathbf{j}$, and collision integral, respectively. The Boltzmann–Curtiss kinetic equation reduces to the original Boltzmann kinetic equation for a monatomic gas when the angular momentum of the molecule due to the rotational mode is completely neglected

$$\left(\frac{\partial f}{\partial t}+\mathbf{v}\cdot\nabla\right)f(\mathbf{v},\mathbf{r},t)=C[f], \tag{4}$$

where $C[f]$ refers to the Boltzmann collision integral of the interaction between two gas molecules.

In gas kinetic theory, the macroscopic variables can be classified into two different groups: conserved variables $(\rho, \rho\mathbf{u}, \rho E)$ and non-conserved variables $(\mathbf{\Pi}, \Delta, \mathbf{Q})$, where $\rho, \mathbf{u}, E$ denote the density, velocity vector, and total energy density, respectively, while $\mathbf{\Pi}, \Delta, \mathbf{Q}$ represent the shear stress tensor, excess normal stress, and heat flux, respectively. These variables can be calculated using the statistical formulation

$$\phi^{(k)}=\langle h^{(k)}f\rangle, \tag{5}$$

where the angular brackets denote the integration of microscopic variables $\mathbf{v}$ and j in the computational domain. $h^{(k)}$ indicates the molecular expression of the h-th moment of the distribution function, and $\phi^{(k)}$ denotes the equivalent macroscopic quantity. The leading elements of the macroscopic set of conserved and non-conserved variables are defined as follows:[36]

$$\begin{gathered}\phi^{(1)}=\rho,\quad \phi^{(2)}=\rho\mathbf{u},\quad \phi^{(3)}=\rho E,\\ \phi^{(4)}=\mathbf{\Pi}=[\mathbf{P}]^{(2)},\quad \phi^{(5)}=\Delta=\frac{1}{3}\,\mathrm{Trace}\,\mathbf{P}-\mathrm{p},\quad \phi^{(6)}=\mathbf{Q}.\end{gathered} \tag{6}$$

The molecular expressions corresponding to this set are as follows:

$$\begin{gathered}h^{(1)}=m,\quad h^{(2)}=m\mathbf{v},\quad h^{(3)}=\frac{1}{3}mC^2+H_{rot},\\ h^{(4)}=[m\mathbf{CC}]^2,\quad h^{(5)}=\frac{1}{3}mC^2-\frac{p}{n},\\ h^{(6)}=\left(\frac{1}{2}mC^2+H_{rot}-m\hat{h}\right)\mathbf{C},\end{gathered} \tag{7}$$

where m is the molecular mass, $\mathbf{C}=\mathbf{v}-\mathbf{u}$ is the peculiar velocity of the molecule, n is the number density per unit mass, $\hat{h}$ is the enthalpy density per unit mass, and $H_{rot}=j^2/2I_m$ is the rotational Hamiltonian of the particle. The symbol $[\mathbf{A}]^{(2)}$ denotes the traceless symmetric part of the second-rank tensor $\mathbf{A}$, given by

$$[\mathbf{A}]^{(2)}=\frac{1}{2}(\mathbf{A}+\mathbf{A}^t)-\frac{1}{3}\mathbf{I}\,\mathrm{Trace}\,\mathbf{A}, \tag{8}$$

where $\mathbf{I}$ denotes the unit second-rank tensor. The viscous shear stresses Pi and excess normal stress Δ are correlated with the stress tensor $\mathbf{P}$ by the relationship

$$\mathbf{P}=(p+\Delta)\mathbf{I}+\mathbf{\Pi}. \tag{9}$$

Here, the pressure p can be calculated by the equation of state, i.e., $p=nk_BT=\rho R_gT$, where n, k_B, T, and R_g denote the number density, Boltzmann constant, absolute temperature, and gas constant, respectively.

The physical conservation laws of mass, momentum, and total energy for diatomic and polyatomic gases can be formulated directly from the Boltzmann–Curtiss kinetic equation by considering the collision-invariant property, where the dissipation term is usually ignored, that is, $\langle h^{(1,2,3)}R[f]\rangle=0$. After differentiating the statistical description of the conserved variables with respect to time and combining them with the Boltzmann–Curtiss equation, the following physical conservation laws for diatomic and polyatomic gases can be derived:

$$\frac{\partial}{\partial t}\begin{bmatrix}\rho\\ \rho\mathbf{u}\\ \rho E\end{bmatrix}+\nabla\cdot\begin{bmatrix}\rho\mathbf{u}\\ \rho\mathbf{uu}+p\mathbf{I}\\ (\rho E+p)\mathbf{u}\end{bmatrix}+\nabla\cdot\begin{bmatrix}0\\ \mathbf{\Pi}+\Delta\mathbf{I}\\ (\mathbf{\Pi}+\Delta\mathbf{I})\cdot\mathbf{u}+\mathbf{Q}\end{bmatrix}=0. \tag{10}$$

In Eq. (10), the symbol E denotes the total energy, which can be defined as follows:

$$E=\frac{1}{(\gamma-1)}\frac{p}{\rho}+\frac{1}{2}\mathbf{u}\cdot\mathbf{u}. \tag{11}$$

The following dimensionless variables and parameters are then considered:

$$\begin{gathered}t^*=\frac{t}{(L/u_r)},\quad \mathbf{x}^*=\frac{\mathbf{x}}{L},\quad \mu^*=\frac{\mu}{\mu_r},\quad k^*=\frac{k}{k_r},\quad \mathbf{u}^*=\frac{\mathbf{u}}{u_r},\\ p^*=\frac{p}{p_r},\quad \rho^*=\frac{\rho}{\rho_r},\quad T^*=\frac{T}{T_r},\quad C_p^*=\frac{C_p}{C_{pr}},\quad E^*=\frac{E}{u_r^2},\\ \mathbf{\Pi}^*=\frac{\mathbf{\Pi}}{(\mu_ru_r/L)},\quad \Delta^*=\frac{\Delta}{(\mu_{br}u_r/L)},\quad \mathbf{Q}^*=\frac{\mathbf{Q}}{k_r\Delta T/L},\end{gathered} \tag{12}$$

where the subscript r denotes the reference state, L denotes the characteristic length, C_p denotes the heat capacity per mass at constant pressure, and μ, μ_b, k are the Chapman–Enskog shear viscosity, bulk viscosity, and thermal conductivity, respectively. The dimensionless physical conservation laws for diatomic and polyatomic gases (with the asterisks removed for notational brevity) can be written as[43,45,48,50–52]

$$\begin{aligned}&\frac{\partial}{\partial t}\begin{bmatrix}\rho\\ \rho\mathbf{u}\\ \rho E\end{bmatrix}+\nabla\cdot\begin{bmatrix}\rho\mathbf{u}\\ \rho\mathbf{uu}+\frac{1}{\gamma M^2}p\mathbf{I}\\ \left(\rho E+\frac{1}{\gamma M^2}p\right)\mathbf{u}\end{bmatrix}\\ &+\frac{1}{Re}\nabla\cdot\begin{bmatrix}0\\ \mathbf{\Pi}+f_b\Delta\mathbf{I}\\ (\mathbf{\Pi}+f_b\Delta\mathbf{I})\cdot\mathbf{u}+\frac{1}{EcPr}\mathbf{Q}\end{bmatrix}=0.\end{aligned} \tag{13}$$

Here, dimensionless parameters such as the Mach number (M), Reynolds number (Re), Eckert number (Ec), and Prandtl number (Pr) are defined as follows:

$$\begin{gathered}M\equiv\frac{u_r}{\sqrt{\gamma R_gT_r}},\quad Re\equiv\frac{\rho_ru_rL}{\mu_r},\quad Ec\equiv(\gamma-1)M^2,\\ Pr\equiv\frac{C_{pr}\mu_r}{k_r},\quad f_b=\frac{\mu_{br}}{\mu_r},\end{gathered} \tag{14}$$

TABLE I. Viscosity ratio f_b for common dilute diatomic and polyatomic gases at 300 K.

Gas	f_b	Gas	f_b	Gas	f_b
Carbon monoxide	0.55	Methane	1.33	Hydrogen	35
Oxygen	0.73	Dimethylpropane	3.27	Chlorine	751.88
Nitrogen	0.80	Water vapor	7.36	Carbon dioxide	1000

where the subscript r denotes the reference state, L denotes the reference length, R_g is the universal gas constant, and C_p denotes the heat capacity per mass at constant pressure. In the present study, the sound speed of a diatomic or polyatomic gas before the shock wave is chosen as the reference velocity u_r, resulting in $M = 1$. Nonetheless, we keep the reference Mach number M in the equations to clarify its role in the formulation. In addition, the bubble radius is used for the reference length, that is, $L = R_b = 25\,\text{mm}$. The dimensionless equation of state is expressed as $\rho_r = P_r/T_r$, where $P_r = 101,325$ Pa and $T_r = 273\,\text{K}$ are used for the reference pressure and temperature, respectively.

The specific heat ratio γ is assumed to be 1.67 for argon, 1.40 for nitrogen, and 1.31 for methane. The factor $f_b = \mu_{br}/\mu_r$ is the ratio of the bulk viscosity to the shear viscosity, and its value can be experimentally calculated based on a sound wave absorption measurement.[39] The viscosity ratios f_b for common dilute diatomic and polyatomic gases at 300 K are listed in Table I. Note that the dilute monatomic gases have a viscosity ratio of zero. The Prandtl number (Pr) can also be determined through Eucken's relationship as

$$Pr = \frac{4\gamma}{9\gamma - 5}. \tag{15}$$

When the statistical definitions of the non-conserved variables $\phi^{(4,5,6)} = \langle h^{(4,5,6)} f \rangle$ are differentiated with respect to time and combined with the Boltzmann–Curtiss equation, the following Navier–Fourier (NF) constitutive equations of the shear stress tensor, excess normal stress, and heat flux vector can be obtained:

$$\mathbf{\Pi} = -2\mu[\nabla \mathbf{u}]^{(2)}, \quad \Delta = -\mu_b \nabla \cdot \mathbf{u}, \quad \mathbf{Q} = -k\nabla T. \tag{16}$$

Moreover, when Stokes' hypothesis [Eq. (2)] is applied, that is, $\mu_b = 0$, the NF constitutive equations in Eq. (16) reduce to the well-known NSF equations. In such expressions, the following Chapman–Enskog linear transport coefficients are used:

$$\mu = T^s, \quad \mu_b = f_b \mu, \quad k = T^s, \tag{17}$$

where s is the index of the inverse power law of gas molecules, given as

$$s = \frac{1}{2} + \frac{2}{\nu - 1}. \tag{18}$$

Here, the parameter ν is the exponent of the inverse power law for the gas–particle interaction potential. The value of s is assumed to be 0.81 for argon, 0.78 for nitrogen, and 0.84 for methane.[59] The physical properties of the tested monatomic, diatomic, and polyatomic gases are listed in Table II.

C. Estimation of bulk viscosity

In this section, we present a detailed overview of the estimation of the bulk viscosity based on the theories of gas kinetics and continuums. In the present work, the only rotational mode is considered to be that which can be excited at room temperature, and therefore ubiquitously over all flow conditions. For this reason, the excitation of the vibrational mode is usually ignored in the study of diatomic and polyatomic gases.

Based on the gas kinetic theory, the bulk viscosity μ_b in single-mode perfect diatomic and polyatomic gases can be mathematically expressed as[60]

$$\mu_b = \frac{pR}{C_v^2} c_{rot} \tau_{rot} = (\gamma - 1) p \frac{c_{rot}}{C_v} \tau_{rot}. \tag{19}$$

Here, C_v is the total specific heat, c_{rot} is the rotational energy mode, and τ_{rot} is the rotational relaxation time, which can be computed easily from Parker's formulas as[61]

$$\tau_{rot} = \frac{\pi}{4} \frac{\mu}{p} Z_{rot}, \tag{20}$$

where Z_{rot} is the rotational collision number defined as

$$Z_{rot} = \frac{Z_{rot}^{\infty}}{1 + \left(\frac{\pi^{3/2}}{2}\right)\sqrt{\frac{T_r}{T}} + \left(\frac{\pi^2}{4} + \pi\right)\frac{T_r}{T}}. \tag{21}$$

For diatomic nitrogen gas, we consider the following parameters: $Z_{rot}^{\infty} = 15.7$, $T_r = 80\,\text{K}$, $c_{rot} = R$, $C_v = 5/2R$. Thus, based on kinetic theory, the bulk viscosity μ_b is estimated as

$$\mu_b = \frac{\pi}{10}(\gamma - 1)\mu Z_{rot}. \tag{22}$$

Consequently, the viscosity ratio f_b is estimated as

$$f_b = \frac{\mu_b}{\mu} = \frac{\pi}{10}(\gamma - 1) Z_{rot}. \tag{23}$$

Using continuum theory, the bulk viscosity can be estimated as[62]

$$\mu_b = K\tau = \gamma p \tau, \tag{24}$$

where K is the isentropic bulk modulus of the fluid,[63] defined as $K = -V(\partial P/\partial V)$, and τ is the average relaxation time. For the rotational mode in a single species, this is defined as

TABLE II. Physical properties of the tested monotonic, diatomic, and polyatomic gases at standard conditions.

Gas	Specific heat ratio (γ)	Prandtl number (Pr)	Viscosity index (s)	Gas constant (R_g)	Viscosity coefficient μ_r
Argon	1.67	0.67	0.81	208.24	2.12×10^{-5}
Nitrogen	1.40	0.74	0.74	296.91	1.65×10^{-5}
Methane	1.31	0.77	0.84	518.24	1.02×10^{-5}

$$\tau = \frac{c_{rot}}{C_v}\tau_{rot}. \tag{25}$$

Therefore, for diatomic nitrogen gas, the bulk viscosity based on continuum theory is estimated to be

$$\mu_b = \frac{\pi}{10}\gamma\mu Z_{rot}, \tag{26}$$

and the corresponding viscosity ratio f_b is

$$f_b = \frac{\mu_b}{\mu} = \frac{\pi}{10}\gamma Z_{rot}. \tag{27}$$

The shear viscosity μ is determined separately according to the inverse power law and Sutherland's law

$$\mu = \begin{cases} \mu_r\left(\dfrac{T}{T_r}\right)^s, & \text{inverse power law,} \\ \mu_r\left(\dfrac{T}{T_r}\right)^{1.5}\left(\dfrac{T_r + T_s}{T + T_s}\right), & \text{Sutherland's law,} \end{cases} \tag{28}$$

where s is the gas viscosity index, μ_r is the gas reference viscosity, and $T_s = 104$ K.

Figure 3 illustrates the temperature variation of the estimated shear viscosity μ, bulk viscosity μ_b, and viscosity ratio f_b for diatomic nitrogen gas. In Fig. 3(a), the computed shear viscosity is compared with the experimental data of Vogel,[66] the theoretical results using the Green–Kubo method,[47] and the computational results of Hanley and Elye[64] and Billing and Wang.[65] The selected potential law replicates

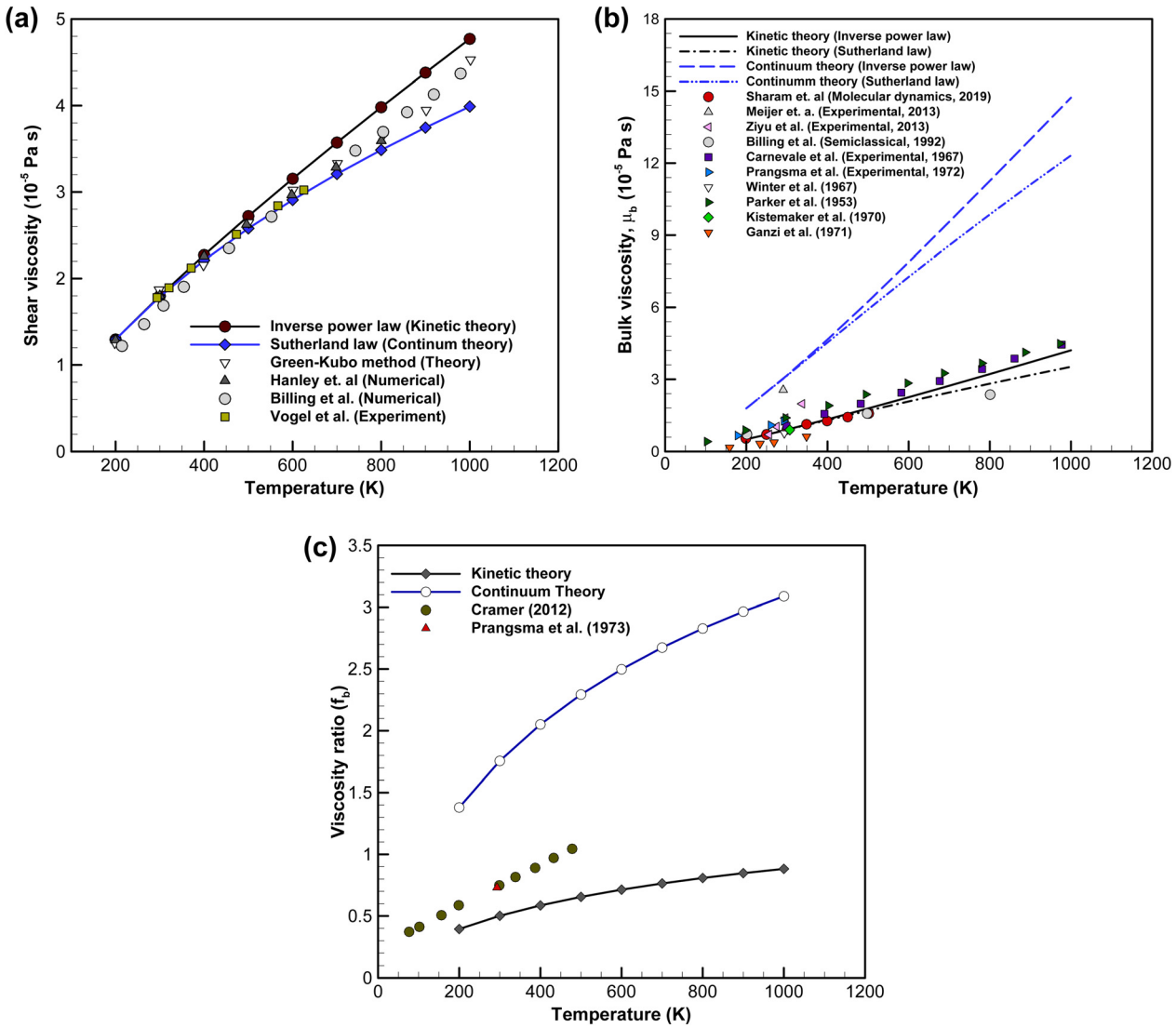

FIG. 3. Temperature variation of (a) shear viscosity μ, (b) bulk viscosity μ_b, and (c) viscosity ratio f_b for nitrogen gas obtained from theories and experiments.

the thermodynamic properties of the simulated gas within an appropriate limit of errors. The estimated bulk viscosity is compared with existing data[61,65,67–71] in Fig. 3(b). Clearly, the bulk viscosity based on kinetic theory is more compatible with the existing data at around 300 K. The viscosity ratio f_b obtained by kinetic theory is also far closer to the experimental data than that obtained by continuum theory, as can be seen in Fig. 3(c). In summary, the general formula for the viscosity ratio is not a fixed constant value, but applies to any temperature through Parker's Z_{rot} model.

D. Initialization of the problem

To initialize the computational simulation for shock-accelerated bubble, we employ the ambient condition on the right-hand side of the shock wave. The primitive variables are calculated on the left-hand side of the shock wave using the Rankine–Hugoniot conditions. The Rankine–Hugoniot conditions for primitive variable calculations are expressed as follows:

$$M_2^2 = \frac{1+\left[\frac{(\gamma-1)}{2}\right]M_s^2}{\gamma M_s^2 - \frac{(\gamma-1)}{2}},$$
$$\frac{p_2}{p_1} = \frac{1+\gamma M_s^2}{1+\gamma M_2^2}, \tag{29}$$
$$\frac{\rho_2}{\rho_1} = \frac{\gamma - 1 + (\gamma+1)\frac{p_2}{p_1}}{\gamma + 1 + (\gamma-1)\frac{p_2}{p_1}}.$$

In the above expressions, M_s denotes the shock Mach number, and the subscripts 1 and 2 denote the left- and right-hand sides of the shock wave, respectively. In the present study, the shock Mach number is set to $M_s = 1.22$.

III. NUMERICAL SCHEME, GRID REFINEMENT, PRECISION ESTIMATION, AND VALIDATION

A. Explicit mixed-type modal discontinuous Galerkin (DG)-based numerical scheme

In recent decades, the discontinuous Galerkin (DG) method has gained widespread popularity as an alternative approach to solving partial differential equations.[51,72–79] In this work, the two-dimensional physical conservation laws [Eq. (13)] for diatomic and polyatomic gases are solved in conjunction with the NF constitutive relations [Eq. (16)] by an explicit mixed-type modal DG solver based on structured meshes that was developed in-house.[32,44,45] The computational domain is discretized into rectangular elements, and scaled Legendre polynomial functions are employed for the elements. The Gauss–Legendre quadrature rule is implemented for both the volume and the boundary integrations, and the Roe flux[80] is applied for the inviscid term. The local DG scheme[78] is employed for the auxiliary and viscous fluxes at the elemental interfaces. A polynomial expansion of third-order accuracy is used to approximate the solutions in the finite element space, and an explicit third-order accurate strong stability preserving Runge–Kutta scheme is used for the time integration. The nonlinear total variation bounded limiter proposed by Cockburn and Shu[79] is used to eliminate spurious numerical fluctuations in the solutions.

To visualize the computational results, numerical schlieren images based on the magnitude of the gradient of the density field are considered[81]

$$S_{i,j} = \exp\left(-k(\phi_{i,j})\frac{|\nabla\rho_{i,j}|}{max_{i,j}|\nabla\rho_{i,j}|}\right), \tag{30}$$

where

$$k(\phi_{i,j}) = \begin{cases} 20 & \text{if } \phi_{i,j} > 0.25, \\ 100 & \text{if } \phi_{i,j} < 0.25. \end{cases}$$

B. Grid refinement analysis

To evaluate the quality of the computational results, grid refinement analysis is performed by computing a test case of a shock-accelerated cylindrical He bubble in N_2 gas at $M_s = 1.22$. Six uniform rectangular meshes are considered. The labels "Mesh 1"–"Mesh 6" correspond to meshes consisting of 100×50, 200×100, 400×200, 800×400, 1200×600, and 1600×800 cells, respectively. When the IS wave hits the bubble surface, the volume of the bubble is compressed and the internal shock waves of the bubble form a divergent shape. Figure 4 shows the density contours for the computed shock-accelerated bubble at time $t = 10$. The numerical results for the rolled-up small-scale vortices are well captured with Mesh 6 (1600×800 cells). Further, the density distribution profiles at the early stage ($t = 1$) along the centerline of the computed bubbles are illustrated in Fig. 5 to demonstrate the grid sensitivity. The results show that Mesh 6 is very close to the asymptotic range. Based on this analysis, all subsequent computations are carried out using Mesh 6.

C. Precision estimation

For large-scale simulations of the complex combustion gas dynamics in unsteady-state flows, it is important to estimate the precision and accumulation of errors. The error depends on accuracy of numerical scheme and grid resolution, and on the number of time steps. For this problem, Smirnov *et al.*[82,83] proposed a method to estimate the error accumulation and simulation precision.

In the one-dimensional case S_1, the relative error of integration is proportional to the mean ratio of the cell size ΔL to the domain size L_1 in the direction of integration in the power, and depends on the accuracy of the scheme

$$S_1 \equiv \left(\frac{\Delta L}{L_1}\right)^{k+1}. \tag{31}$$

For a uniform grid, $S_1 \equiv (1/N_1)^{k+1}$, where N_1 is the number of cells in the direction of integration and k is the order of accuracy of the numerical scheme. The errors provided by Eq. (31) in two directions are being summed up

$$S_{err} \equiv \sum_{i=1}^{2} S_i. \tag{32}$$

The allowable value of the total error $S_{\max}$ is typically 1%–5%, because the initial and boundary conditions are usually not known with a

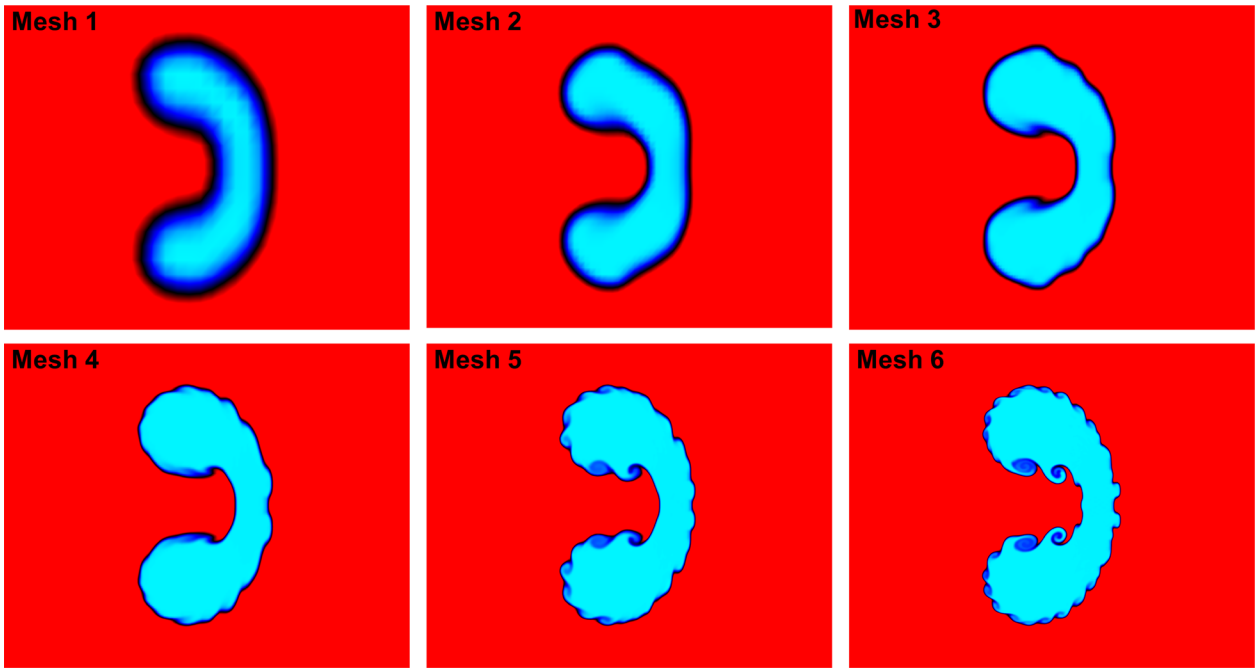

FIG. 4. Grid refinement study: contours of density distribution with different mesh sizes for shock-accelerated cylindrical He bubble surrounded by nitrogen gas at time $t = 10$.

higher degree of accuracy. As a result, the following inequality should be satisfied:

$$S_{err} \cdot \sqrt{n} \leq S_{\max}, \tag{33}$$

where n is the number of time steps. The maximal allowable number of time steps can then be determined by the following formula:

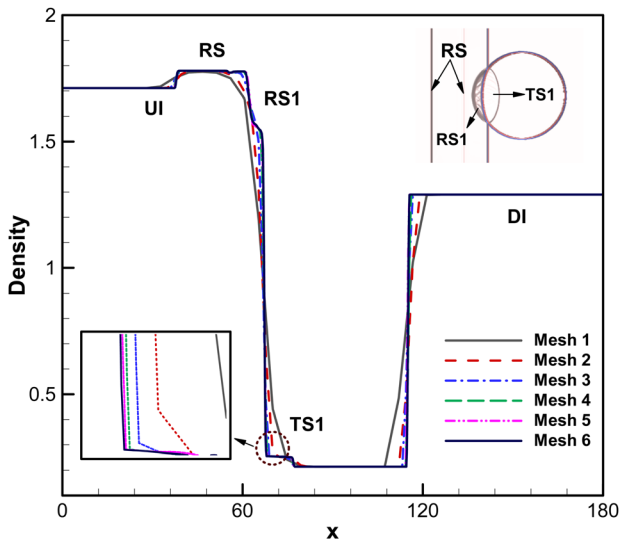

FIG. 5. Grid refinement study: profiles of density distribution along the centerline of computed bubble at time $t = 1$. The symbols UI, DI, RS, TS1, and RRW1 denote the upstream interface, downstream interface, reflected shock wave, first-transmitted shock wave, and first-reflected rarefaction wave, respectively.

$$n_{\max} = \left(\frac{S_{\max}}{S_{err}}\right)^2, \tag{34}$$

and the reliability of results can be defined as

$$R_s = \frac{n_{\max}}{n}. \tag{35}$$

Table III predicts the accumulation of errors for the present DG scheme with different grid resolutions. The allowable error is considered to be 5%, and the final simulation time is set to 5. As can be seen, the errors accumulate rapidly for the coarse grid and decrease as the grid resolution increases. The reliability of the results increases with a higher grid resolution and scheme accuracy. For the present simulations, all results demonstrate that the computational model is highly reliable, but this may not be the case for longer simulation periods.[82,83]

D. Validation of the numerical solver

To verify the reliability and accuracy of the present computational model and numerical DG solver, the obtained results are compared with the experimental results of Hass and Sturtevant[13] and the computational results of Quick and Karni,[20] in which the cylindrical gas bubble was filled with refrigerant-22 (R_{22}) and the ambient zone was composed of air. The aforementioned experimental and computational studies also had a weak shock with $M_s = 1.22$. Figure 6 compares the schlieren images between the experimental results,[13] computational results,[20] and the present numerical results at different times. These numerical simulations share the same initial condition, resolution, and diffusion layer thickness. As seen from Fig. 6, the schlieren images are in good agreement across all experimental and computational results, with the vortex structures resembling one

TABLE III. Error estimation.

Allowable error (%)	Grid resolution	Time simulated	Number of time steps	Accumulated error	Allowable number of time steps	Reliability ($R_s = n_{max}/n$)
5	100×50	5	53	2.60×10^{-4}	36 982	698
5	200×100	5	107	9.47×10^{-5}	2.79×10^{5}	2.61×10^{3}
5	400×200	5	209	3.44×10^{-5}	2.11×10^{6}	1.01×10^{4}
5	800×400	5	419	1.26×10^{-5}	1.57×10^{7}	3.76×10^{4}
5	1200×600	5	634	7.19×10^{-6}	4.84×10^{7}	7.63×10^{4}
5	1600×800	5	845	1.59×10^{-6}	9.89×10^{8}	1.17×10^{6}

another. Furthermore, Fig. 7 shows the space–time diagram for the characteristic interface points [i.e., upstream interface (UI), downstream interface (DI), and inward-jet head (jet)]. The numerical results are in good agreement with the experimental results.[13] The positions and speeds of the various shock waves and the interfaces are accurately simulated by the computational model.

The velocities of these characteristic interface points (V_{DI}, V_{UI}, and V_{Jet}), together with the time intervals involved in their computation, are presented alongside those obtained by Hass and Sturtevant[13] and Quick and Karni[20] in Table IV. These velocities are estimated during the propagation inside the bubble and taken along the $x-$direction of the centerline of the domain. The discrepancy between the experimental, computational, and simulated velocities can be seen in Fig. 7, where the characteristic interface points do not exactly coincide. These discrepancies could be caused by the current numerical model ignoring the mass fraction term.

Further, the current computational model is also validated through a comparison with the three-dimensional experimental work of Ding *et al.*[84] Figure 8 shows schlieren images of the experimental results of Ding *et al.*[84] and the present numerical (two-dimensional) results for a three-dimensional convex N_2 cylinder surrounded by SF_6 with $M_s = 1.29$ at selected time instants. The evolved shock wave patterns and the convex

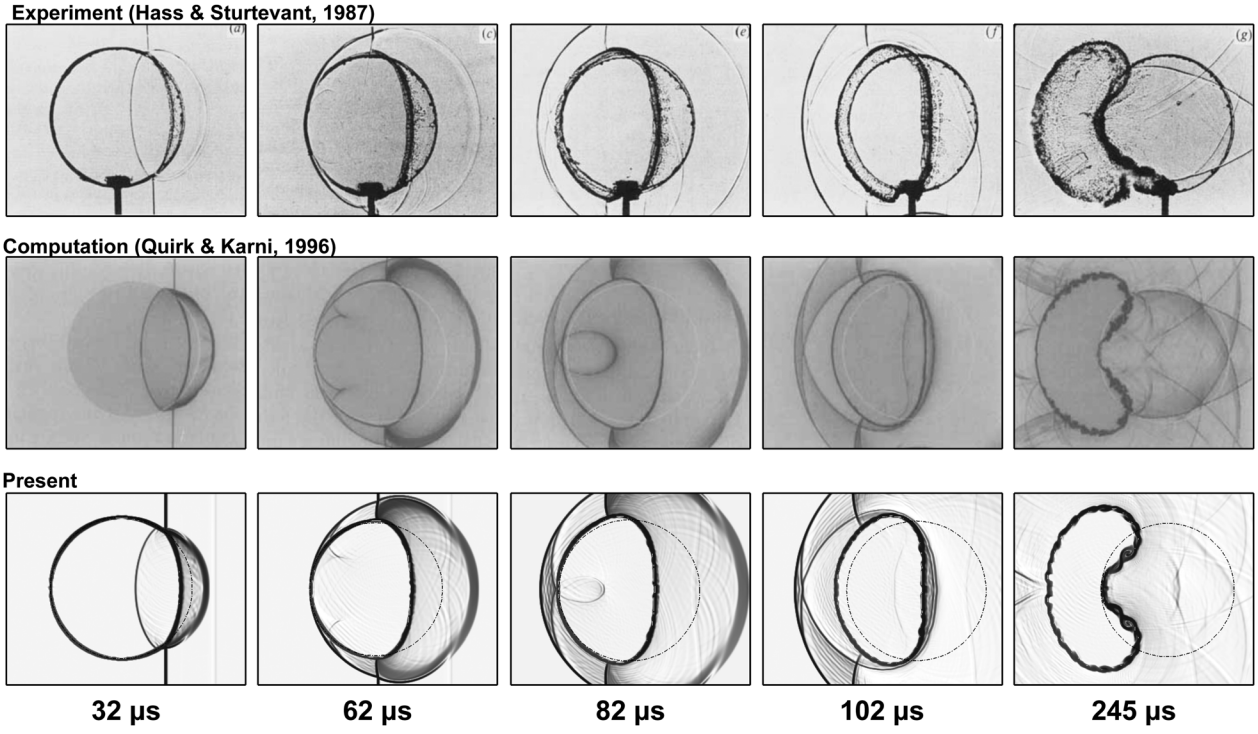

FIG. 6. Validation of the numerical solver: comparison of numerical schlieren images between the experimental results [reproduced with permission from J. F. Haas and B. Sturtevant, J. Fluid Mech. **181**, 41–76 (1987). Copyright 1987 Cambridge University Press],[13] the computational results [reproduced with permission from J. J. Quirk and S. Karni, J. Fluid Mech. **318**, 129–163 (1996). Copyright 1996 Cambridge University Press],[20] and the present numerical results for a shock-accelerated R_{22} cylindrical bubble surrounded by air at different time instants.

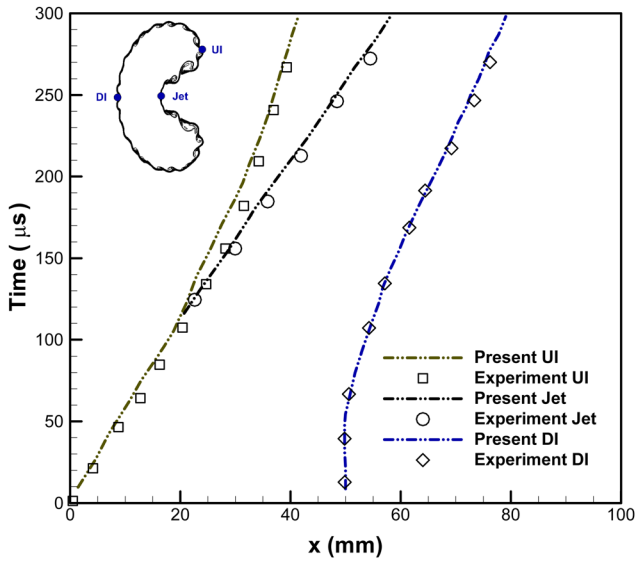

FIG. 7. Validation of the numerical solver: comparison of computed characteristic interface points (UI, DI, and Jet) between the experimental results [reproduced with permission from J. F. Haas and B. Sturtevant, J. Fluid Mech. **181**, 41–76 (1987). Copyright 1987 Cambridge University Press][13] and the present numerical results for a shock-accelerated R_{22} cylindrical bubble surrounded by air. The definitions of the characteristic interface points are inserted.

cylinder shape are in good agreement at these time instants, indicating that the current numerical model is sufficiently accurate.

IV. RESULTS AND DISCUSSION: SHOCK-ACCELERATED CYLINDRICAL LIGHT BUBBLE IN DIATOMIC AND POLYATOMIC GASES

In this section, the flow morphology of the shock-accelerated cylindrical light bubble in diatomic and polyatomic gases is investigated. The impacts of an initial interface perturbation on the flow morphology, wave patterns, vorticity distribution, interface movements, and qualitative analysis are emphasized. An incident shock wave with $M_s = 1.22$ is selected for the numerical simulations. Helium is used as the bubble gas; this has been widely adopted as the light gas in studies of the RM instability. To investigate the flow morphology of shock-accelerated cylindrical He bubble in diatomic and polyatomic gases, three different types of gases—argon, nitrogen, and methane—are considered as the gas surrounding the bubble. The physical properties of these gases are summarized in Table II, and the Atwood number for each ambient gas–bubble gas configuration is listed in Table V.

TABLE IV. Validation of the numerical solver: comparison of velocities of characteristic interface points between experimental data,[13] computational data,[20] and the present numerical data. V_{DI}: velocity of downstream interface; V_{UI}: velocity of upstream interface; V_{Jet}: velocity of inward-jet head.

Velocity (m/s)	Present	Experimental	% error	Computational	% error
V_{DI}	148	145	−2.07	146	−1.37
V_{UI}	175	170	−2.86	178	1.67
V_{Jet}	228	230	0.87	227	−0.44

This section is divided into three parts. First, the overall flow morphology of a shock-accelerated cylindrical He bubble in nitrogen gas is discussed in depth. The impacts of diatomic and polyatomic gases on the flow morphology of the shock-accelerated cylindrical He bubble are then systematically investigated to highlight the differences in comparison with monatomic gases. This investigation includes flow morphology visualization, vorticity generation, degree of thermal nonequilibrium, enstrophy, and dissipation rate. Quantitative analysis based on the shock trajectories and interface features provides a deeper understanding of the effects of diatomic and polyatomic gases. Finally, the impacts of bulk viscosity on the dynamics of the shock-accelerated bubble are investigated.

A. Visualization of overall flow morphology

Visualization of the flow evolution is considered the most interesting phenomenon during the interaction between an IS wave and a gas bubble. To understand this phenomenon, we conducted an extensive investigation of the time evolution of flow morphology for the shock-accelerated cylindrical He bubble. Figure 9 illustrates a sequence of density contours and numerical schlieren images for a cylindrical He bubble surrounded by nitrogen gas ($f_b = 0.8$) accelerated by a planar IS wave with $M_s = 1.22$ at different time instants. Before interacting with the IS wave, the initial state of the bubble interface can be clearly observed ($t = 0$). When the IS wave reaches the bubble interface, the bubble begins to compress. In addition, a transmitted shock wave (TS1) propagating downstream inside the bubble is generated, while a reflected shock wave (RS1) simultaneously travels upstream ($t = 1$). This process is known as the first step of the reflection–transmission process. The propagation speed of the IS wave inside the bubble is smaller than that in the surrounding gas due to the small acoustic impedance. Therefore, the generated TS1 inside the bubble travels faster behind the IS wave. As the interaction develops, the IS and TS1 waves form a quadruple shock in the gas, which reveals irregular refraction. As a consequence, a Mach reflection configuration is generated with a Mach stem (MS), triple point (TP), and slip surface (SS), as can be seen at $t = 2$. Later, a secondary transmitted shock wave (TS2) is observed near the downstream interface ($t = 2.5$). As TS1 crosses the middle region of the bubble, a second reflected shock wave (RS2) is generated in the bubble upstream. This is produced by the deformed interface due to the difference in acoustic impedance of the internal and external gases ($t = 3.5$), which can be considered as the second step of the reflection–transmission process.

As time proceeds, another reflected shock wave (RS3) within the bubble moves upward and then hits the upstream interface, generating a third transmitted shock wave (TS3) at $t = 4.5$, known as the third step of the reflection–transmission process. Simultaneously, the flow fields become more complicated near the downstream interface, and a fourth transmitted shock wave (TS4) appears ($t = 4.5$). During the interaction, the bubble is gradually deformed. The density inhomogeneity is accelerated at the very beginning, and the upstream bubble interface is flat ($t = 1 - 3.5$). The evolving bubble interface then starts to transform into a mushroom shape at $t = 4.5$, and a reentrant gas jet head is subsequently generated near the center of the bubble ($t = 6$). As time proceeds, the jet catches up with the downstream bubble interface, and then, a pair of vortex rings (VR) connected with a bridge

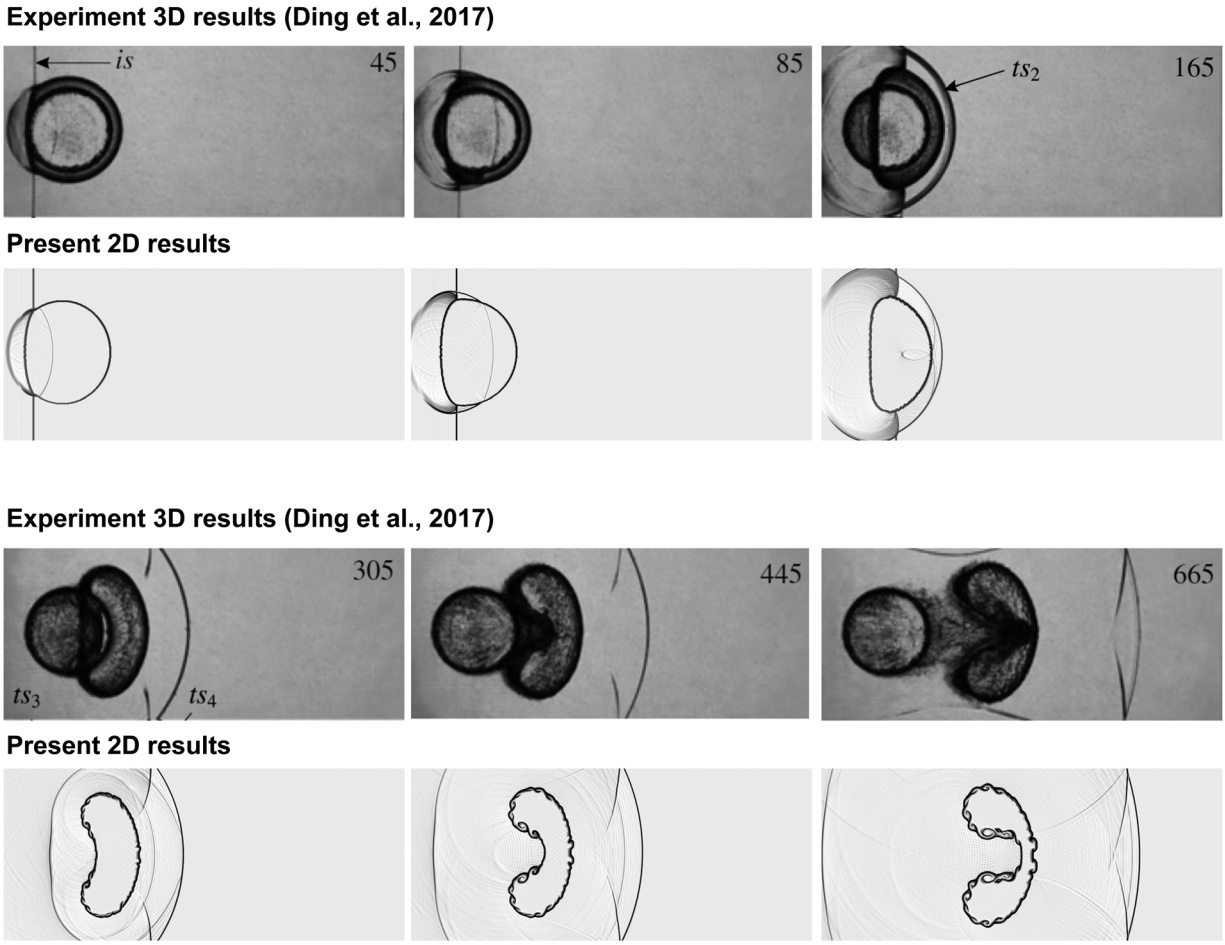

FIG. 8. Validation of the numerical solver: comparison of numerical schlieren images between the experimental three-dimensional results [reproduced with permission from Luo *et al.*, J. Fluid Mech. **828**, 289 (2017). Copyright 2017 Cambridge University Press][84] and the present numerical (two-dimensional) results for a three-dimensional convex N_2 cylinder surrounded by SF_6 with $M_s = 1.29$ at different time instants.

(B) emerges and grows almost symmetrically $(t = 10 - 20)$. Eventually, the flow field is completely controlled by the VR.

B. Effects of diatomic and polyatomic gases on shock-accelerated cylindrical He bubble

1. Flow morphology visualization

Figure 10 demonstrates the impacts of diatomic and polyatomic gases on the flow morphology in the shock-accelerated cylindrical He bubble at various time instants. In all three cases, a Mach reflection configuration, including four transmitted shock waves (TS1, TS2, TS3, and TS4) and three reflected rarefaction waves (RSW1, RSW2, and RSW3), is formed due to the intense interaction between the IS wave and the cylindrical bubble. In argon gas $(f_b = 0)$, the interaction process is sluggish and weak due to the high density of the ambient gas, as shown in Fig. 10(a). As the IS wave passes, the multiple transmitted shock waves and reflected rarefaction waves appear during the interaction process. Subsequently, a reentrant gas jet head is found in the centerline near the right interface of the bubble. In the case of nitrogen gas $(f_b = 0.8)$, the interaction process is stronger, and the reentrant gas jet is larger than with argon, as shown in Fig. 10(b). In addition, the size and strength of the rolled-up vortices increase significantly, and these vortices are conspicuous at the interface between the bubble and surrounding gas due to the baroclinic vorticity deposition. In methane gas $(f_b = 1.33)$, certain areas near the bubble interface become larger after a long time, as shown in Fig. 10(c). Moreover, the expansion of the reflected rarefaction waves can be observed in these larger regions. The size of the rolled-up vortices increases and the

TABLE V. Atwood number (A_t) for ambient gas–bubble configurations.

Ambient gas–bubble configuration	ρ_g (kg/m^3)	ρ_b (kg/m^3)	A_t
Argon–Helium	1.78	0.16	−0.80
Nitrogen–Helium	1.25	0.16	−0.77
Methane–Helium	0.72	0.16	−0.64

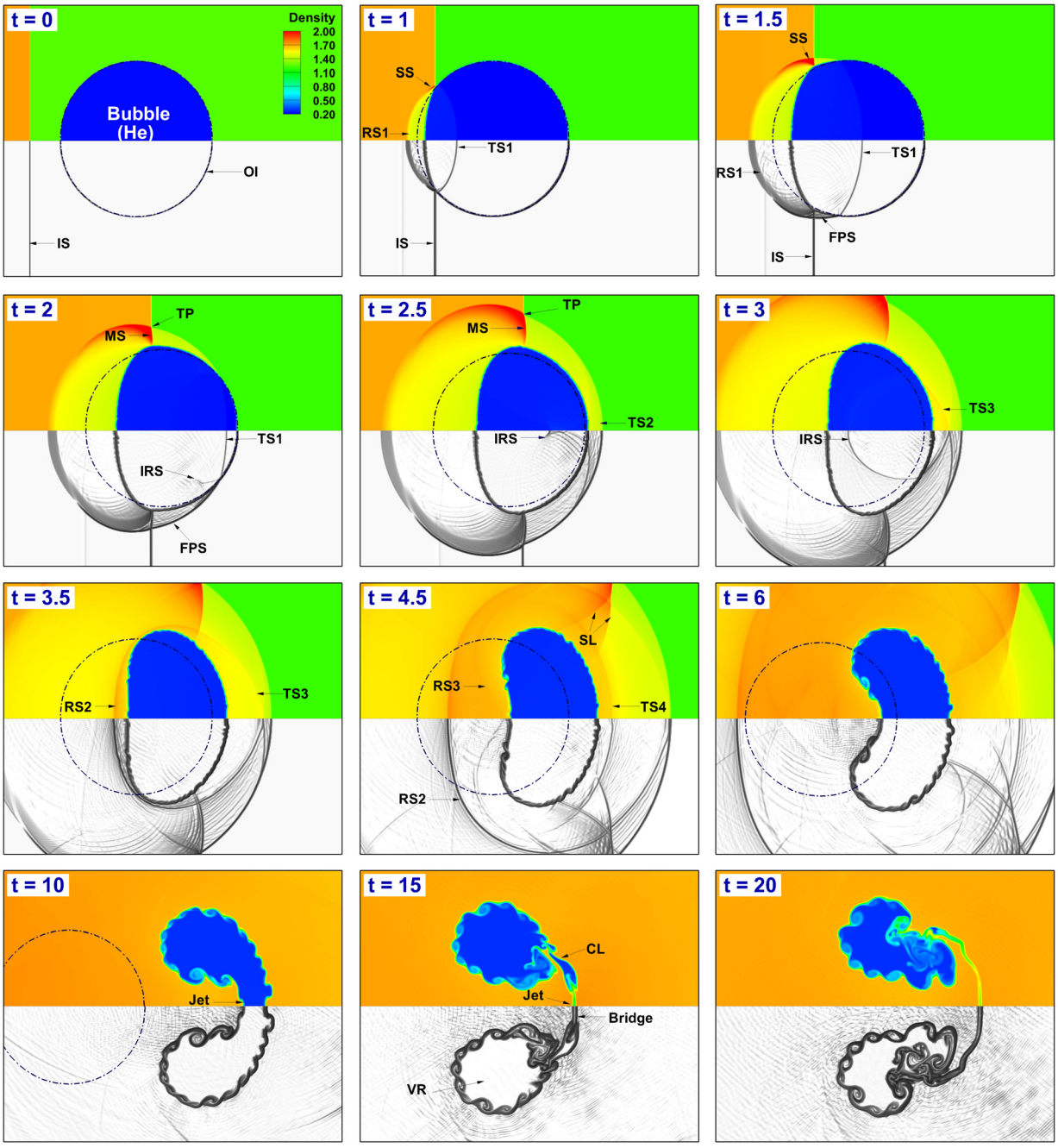

FIG. 9. Visualization of overall flow morphology of the shock-accelerated cylindrical He bubble in nitrogen gas: time evolution of density contour (top) and numerical schlieren images (bottom).

connecting bridge between the generated vortex pair becomes narrower. Interestingly, a thick He inward reentrant gas jet is generated in argon gas, while a different kind of thin He inward reentrant gas jet is formed in nitrogen and methane due to the second instabilities. Later, the He jet becomes vertically elongated with a weaker head because of the diffusion and mixing of the two gases, and the interface develops strong vortex rings ($t = 13$). Because of the Kelvin–Helmholtz instability, the interface then breaks up, resulting in a slew of small-scale structures.

Further, the evolution of the bubble shape during the interaction with the IS wave, shown in Fig. 11, illustrates the effects of diatomic and polyatomic gases on the shock-accelerated cylindrical He bubble. The bubble appears to be compressed by the IS wave along the $x-$ direction, and, compared with its middle section, the top and bottom

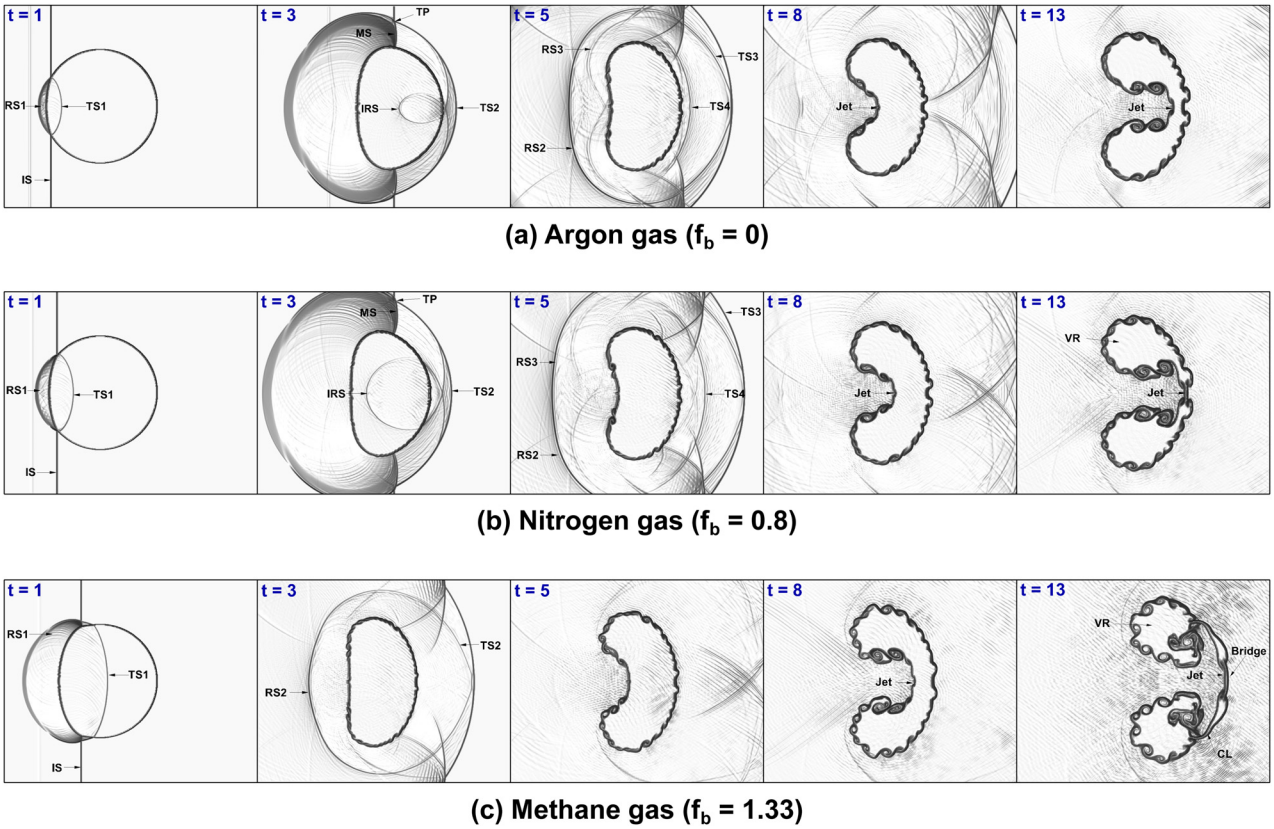

FIG. 10. Effects of diatomic and polyatomic gases on the shock-accelerated cylindrical He bubble: numerical schlieren images in (a) argon gas ($f_b = 0$), (b) nitrogen gas ($f_b = 0.8$), and (c) methane gas ($f_b = 1.33$) at different time instants.

edges have been pushed forward near the horizontal axis of symmetry. At the beginning of the interaction, this compression starts as soon as the IS wave hits the upstream end of the bubble. For all three gases, both the upstream and downstream interfaces travel fast, and the middle section of the upstream interface is initially pressed inward under the influence of the IS wave, as shown in Figs. 11(a)–11(c). Over time, the upper and lower interfaces of the bubble fold inward toward the upstream axis, and the bubble deforms into a divergent shape. Some small-scale rolled-up vortices are generated on the upper and lower interfaces due to baroclinic vorticity generation. In the case of argon gas, the rolled-up vortices are relatively small. These rolled-up vortices are continuously increasing over time. At later stages, the flow field is completely controlled by the rolled-up vortices. Different types of inward jet-head can be observed near the downstream boundary for each ambient gas, although these gradually disappear with time, as shown in Figs. 11(a)–11(c). Eventually, the flow field is completely controlled by the vortex pairs.

2. Dynamics of vorticity generation

In the investigation of a shock-accelerated bubble, the vorticity due to the misalignment of the pressure and the density gradients plays a vital role in understanding the flow morphology phenomena during the interaction process. We now look at how the baroclinic vorticity term affects the IS and TS1 waves as they pass through the stationary bubble interface early in their evolution. In the shock-accelerated bubble, the dominant pressure gradient occurs in the plane IS wave, while the dominant density gradient can be found at the bubble interface. When the plane IS wave passes over the bubble, it does not deform the bubble significantly. The resulting vorticity lies on the bubble interface and has a sinusoidal distribution of magnitude with maxima at the top and bottom edges of the bubble, decreasing to zero at the front and back edges. A schematic diagram of the vorticity generation on the bubble interface after the initial IS wave transits across the light gas bubble is illustrated in Fig. 12. As the pressure and density gradients are perfectly aligned at the upper and lower interfaces, a small quantity of vorticity is generated at the upper and lower interfaces by the IS wave. As the IS wave propagates along the upper and lower interfaces, Mach reflection occurs, in which the Mach stem (MS) connects the IS wave with the interfaces. Therefore, the MS contributes to the pressure gradient that causes vorticity generation on the interface, and the baroclinic vorticity term is thus gradually triggered as the IS wave travels upward over the interfaces.

Figure 13 illustrates the effects of the diatomic and polyatomic gases on the vorticity distribution of the shock-accelerated cylindrical He bubble at different time instants. Initially, the vorticity is equal to zero everywhere. As the IS wave passes across the bubble, the baroclinic vorticity is deposited locally on the bubble interface, where the

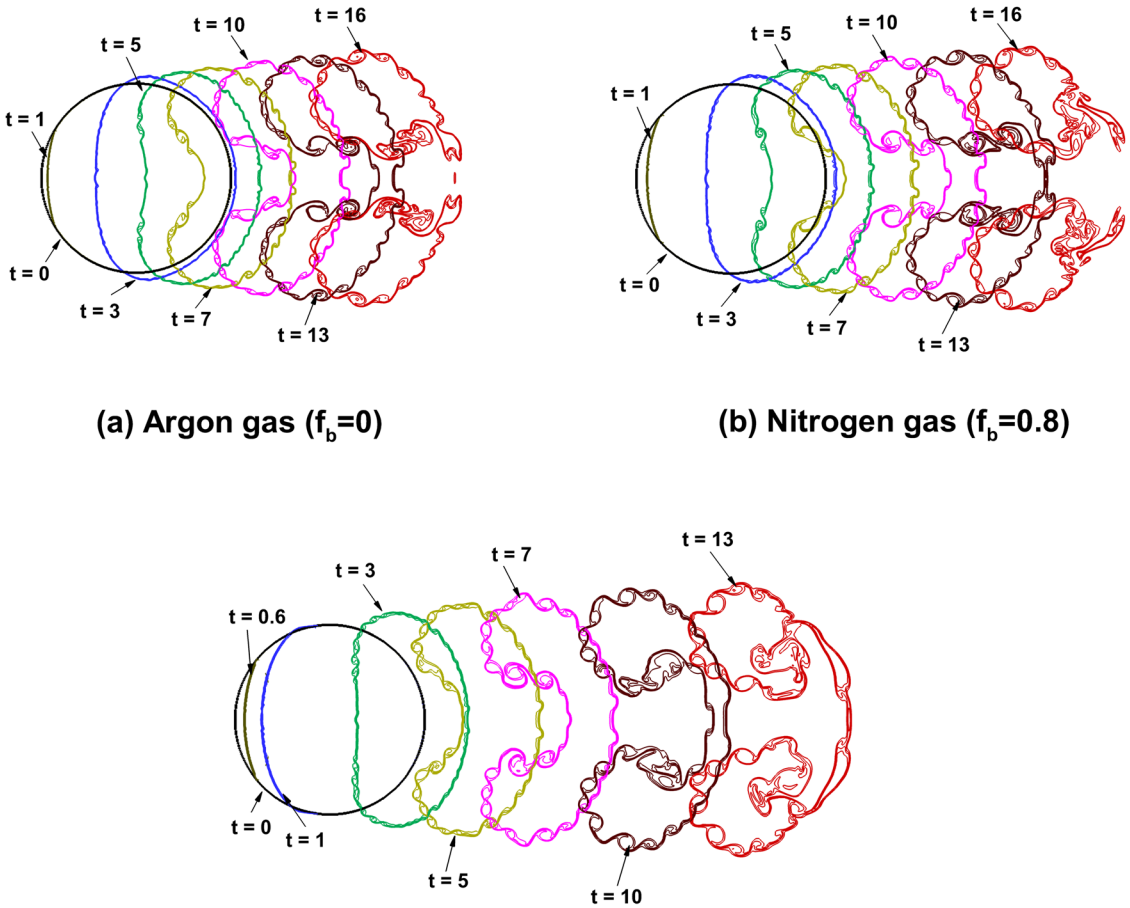

FIG. 11. Effects of diatomic and polyatomic gases on the shock-accelerated cylindrical He bubble: evolution of the bubble shape showing early compression in (a) argon gas ($f_b = 0$), (b) nitrogen gas ($f_b = 0.8$), and (c) methane gas ($f_b = 1.33$).

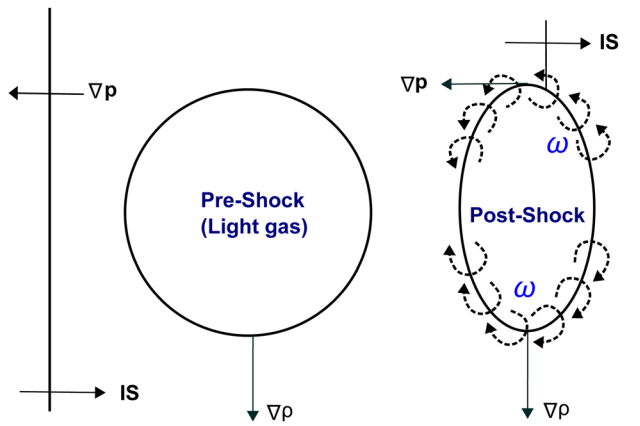

FIG. 12. Schematic diagram of the vorticity generation on the interface of a cylindrical light bubble during and after initial shock wave transit.

discontinuity between the He gas and the ambient gas exists. At the top and bottom interfaces of the bubble, where the density and pressure gradients are orthogonal, the vorticity attains its maximum magnitude; at the regions of the interface where the density and pressure gradients are collinear, the vorticity is zero. A significant quantity of positive vorticity is generated along the upper half of the bubble interface, and a significant quantity of negative vorticity is generated along the lower half of the bubble interface, as shown in Figs. 13(a)–13(c). This is because the IS wave propagates from left to right along the bubble interface. As a result, the density gradient is directed radially outward everywhere along the bubble interface and the pressure gradient acts across the upstream IS wave. After passing the bubble, the transmitted shock wave produces a small quantity of vorticity in the filaments connecting the rolled-up vortices. Some negative (positive) vorticity is concentrated on the upper-half (lower-half) plane of the generated inward jet head. It can be observed that there are substantial gaps in the vorticity distribution for the various gases after the interaction. For argon gas, a small quantity of vorticity is generated around

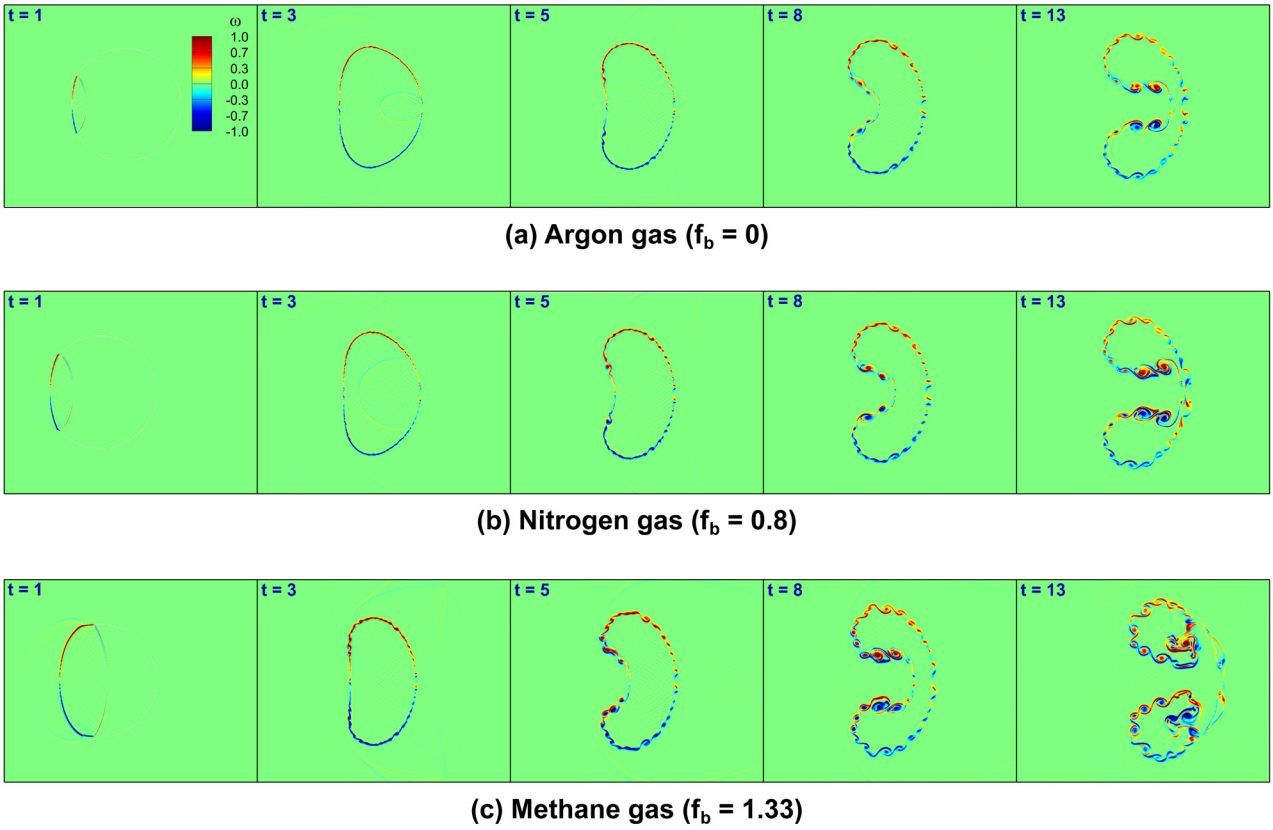

FIG. 13. Effects of diatomic and polyatomic gases on the shock-accelerated cylindrical He bubble: contours of vorticity distribution in (a) argon gas ($f_b = 0$), (b) nitrogen gas ($f_b = 0.8$), and (c) methane gas ($f_b = 1.33$) at different time instants.

the rolled-up vortices on the bubble interface, as shown in Fig. 13(a). These rolled-up vortices are more pronounced for nitrogen and methane, as seen in Figs. 13(b) and 13(c). In summary, the generation and distribution of vorticity play a dominant role in the diatomic and polyatomic gases when rolled-up vortices are formed.

The vorticity on the bubble interface plays a crucial role in gas mixing inside and outside the bubble. Therefore, to obtain a better understanding of the physics of vorticity generation in diatomic and polyatomic gases, four important spatially integrated fields are investigated in detail: (i) average vorticity (ω_{av}), (ii) absolute dilatation vorticity ($|\omega_{dil}|$), (iii) absolute baroclinic vorticity ($|\omega_{bar}|$), and (iv) absolute viscous vorticity ($|\omega_{vis}|$). The spatially integrated field of average vorticity is defined as follows:

$$\omega_{av}(t) = \frac{\int_D |\boldsymbol{\omega}| dxdy}{\int_D dxdy}, \tag{36}$$

where D represents the entire computational domain. The spatially integrated field of absolute dilatation vorticity is computed as follows:

$$|\omega_{dil}|(t) = -\int_D |\boldsymbol{\omega}(\nabla \cdot \mathbf{u})| dxdy. \tag{37}$$

The spatially integrated field of absolute baroclinic vorticity is given by

$$|\omega_{bar}|(t) = \int_D |\frac{1}{\rho^2}(\nabla\rho \times \nabla p)| dxdy. \tag{38}$$

Finally, the spatially integrated field of absolute viscous vorticity is defined as

$$|\omega_{vis}|(t) = \int_D |\boldsymbol{\omega}_{\text{viscous}}| dxdy, \tag{39}$$

where

$$\begin{aligned}\boldsymbol{\omega}_{\text{viscous}} = {} & \frac{\mu}{\rho}\nabla^2\boldsymbol{\omega} - \frac{\mu}{\rho^2}(\nabla\rho \times \nabla^2\mathbf{u}) - \left(\frac{1}{3}+f_b\right)\frac{\mu}{\rho^2}\nabla\rho \\ & \times \nabla(\nabla\cdot\mathbf{u}) + \frac{1}{\rho}(\nabla\mu\cdot\nabla)\boldsymbol{\omega} + \frac{1}{\rho}(\boldsymbol{\omega}\cdot\nabla)\nabla\mu - \frac{\boldsymbol{\omega}}{\rho}\nabla^2\mu \\ & + \frac{1}{\rho}\nabla\mu \times \nabla^2\mathbf{u} + \frac{2}{\rho}\nabla(\nabla\mu\cdot\nabla)\times\mathbf{u} - \frac{1}{\rho^2}\nabla\rho\times(\nabla\mu\times\boldsymbol{\omega}) \\ & - \frac{2}{\rho^2}\nabla\rho\times(\nabla\mu\cdot\nabla)\mathbf{u} + \left(\frac{2}{3}-f_b\right)\frac{(\nabla\cdot\mathbf{u})}{\rho^2}\nabla\rho \\ & \times\nabla\mu + \frac{1}{\rho}\nabla\mu\times\nabla(\nabla\cdot\mathbf{u}).\end{aligned}$$

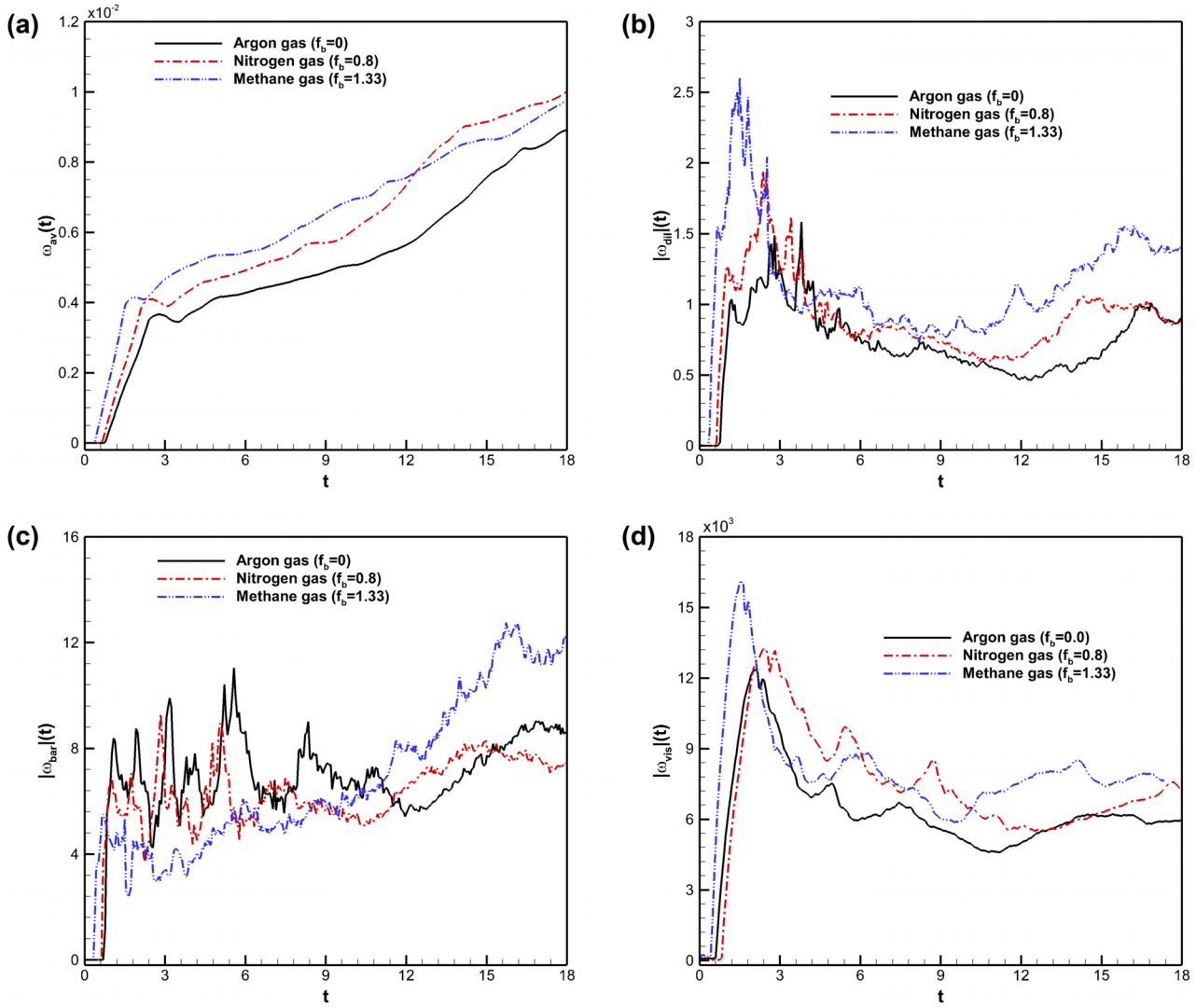

FIG. 14. Effects of diatomic and polyatomic gases on the shock-accelerated cylindrical He bubble: spatially integrated fields of (a) average vorticity (ω_{av}), (b) absolute dilatational vorticity ($|\omega_{dil}|$), (c) absolute baroclinic vorticity ($|\omega_{bar}|$), and (d) absolute viscous vorticity ($|\omega_{vis}|$).

Figure 14 illustrates the effects of diatomic and polyatomic gases on the spatially integrated fields of average vorticity, absolute dilatational vorticity, absolute baroclinic vorticity, and absolute viscous vorticity in the shock-accelerated cylindrical He bubble. It can be observed that argon gives the smallest values of these spatially integrated fields when the incident and reflected shock waves collide with the bubble. The spatially integrated fields are substantially enhanced in the case of methane gas. For all three gases, the spatially integrated fields increase with time, which implies that the ambient gas is increasingly entrained into the distorted cylindrical He bubble. The vortices produced by the shock wave–bubble interaction encourage the mixing of ambient gas with the cylindrical He bubble. When the reflected shock waves impinge on the distorted He bubble again, the spatially integrated fields exhibit their greatest growth rate, which indicates that the vorticities are significantly enhanced during this period, as shown in Fig. 14. The growth rate then slows under the influence of the higher viscosity in the flow field. As a result, the evolution of the spatially integrated fields for vorticity and its associated components does not exhibit a simple monotonic relationship with the ambient gas.

3. Degree of thermal nonequilibrium

In the theory of irreversible thermodynamics, the degree of thermal nonequilibrium based on Rayleigh–Onsager theory[85] is a vital component and is directly related to entropy production in nonequilibrium processes. To demonstrate the degree of thermal nonequilibrium, the Rayleigh–Onsager dissipation function (R) is defined as follows:[43,50]

$$R^* = \frac{\gamma M^2/Re}{p^*}\left[\mathbf{\Pi}^* : \mathbf{\Pi}^* + 2\gamma' f_b \Delta^{*2} + \frac{2}{EcPr}\frac{\mathbf{Q}^* \cdot \mathbf{Q}^*}{T^*}\right]^{1/2}, \quad (40)$$

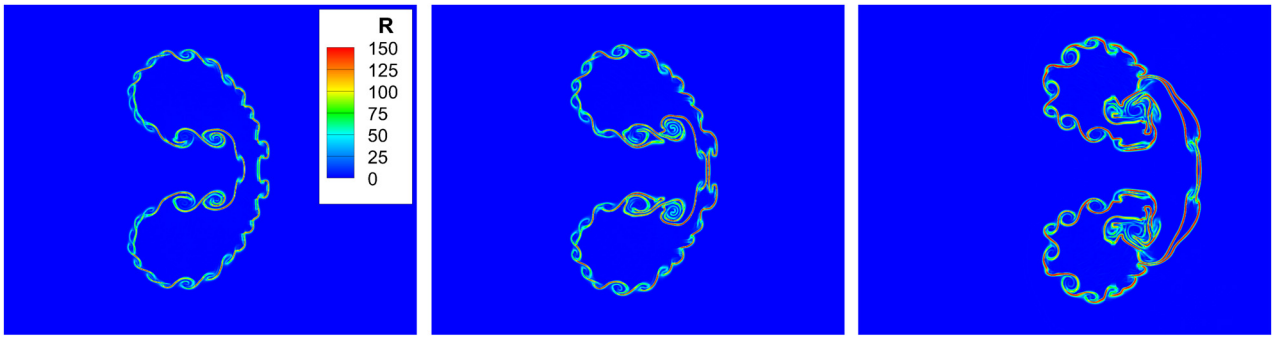

FIG. 15. Effects of diatomic and polyatomic gases on the shock-accelerated cylindrical He bubble: contours of degree of thermal non-equilibrium (R) for (a) argon gas ($f_b = 0$), (b) nitrogen gas ($f_b = 0.8$), and (c) methane gas ($f_b = 1.33$) at time $t = 12$.

where $\gamma' = (5 - 3\gamma)/2$. The symbols $\mathbf{\Pi}^*$, Δ^*, and $\mathbf{Q}^*$ denote the viscous stress, excess normal stress, and heat flux, respectively.

In the shock-accelerated bubble, the mathematical expression of R defined in Eq. (40) measures the regions of the bubble interface that deviate significantly from the local equilibrium state. Figure 15 illustrates the contours of the degree of thermal nonequilibrium at time instant $t = 12$ when the IS wave collides with the bubble interface. The contours of the degree of thermal nonequilibrium depict the regions where the flow experiences sudden changes and the degree of nonequilibrium is higher than in other parts of the computational domain. A higher degree of thermal nonequilibrium is observed at the bubble interface, where the interaction produces the most visible nonequilibrium (as high as $R = 150$). The numerical results show that the degree of nonequilibrium is much higher for diatomic and polyatomic gases than for monatomic gases. The reason behind this physical phenomenon is the presence of significantly higher values of the viscous stress, excess normal stress, and heat flux in diatomic and polyatomic cases. To obtain a better understanding of the effects of diatomic and polyatomic gases on the shock-accelerated cylindrical He bubble, the degree of thermal nonequilibrium can be explained based on the spatially integrated fields during the interaction. Figure 16 depicts the spatially integrated fields of the degree of thermal nonequilibrium. The results reveal that, during the interaction, the degree of thermal nonequilibrium rises significantly in diatomic and polyatomic gases.

4. Enstrophy and dissipation rate

The physical phenomena of vorticity generation during the interaction can be further explained by measuring the time evolution of the enstrophy. The time evolution of the enstrophy can be defined as the area integral of the square of the vorticity in the flow field

$$\Omega(t) = \int_D \omega^2 dxdy. \tag{41}$$

Moreover, the viscous effects of diatomic and polyatomic gases can be investigated by introducing the area-weighted dissipation rate of kinetic energy

$$\epsilon(t) = \int_D E(x, y, t) dxdy, \tag{42}$$

where $E(x, y, t)$ represents the dissipation rate per unit volume, which is defined as

$$E(x, y, t) = -((\Pi_{xx} + f_b\Delta)S_{xx} + \Pi_{xy}S_{xy} + \Pi_{yx}S_{yx} + (\Pi_{yy} + f_b\Delta)S_{yy}). \tag{43}$$

Here, Π_{ii} is the viscous shear stress, Δ is the excess normal stress, and S_{ij} is the strain rate, defined as $S_{ij} = \partial u_i/\partial x_j$.

Figure 17 illustrates the effects of diatomic and polyatomic gases on the enstrophy and dissipation rate in the shock-accelerated cylindrical He bubble at time $t = 12$. There are significant differences in enstrophy and dissipation rate for the different gases after the interaction. Higher values of the enstrophy and dissipation rate are found inside the rolled-up vortices of the deformed bubble interface. In comparison with monatomic gases, the enstrophy and dissipation rate

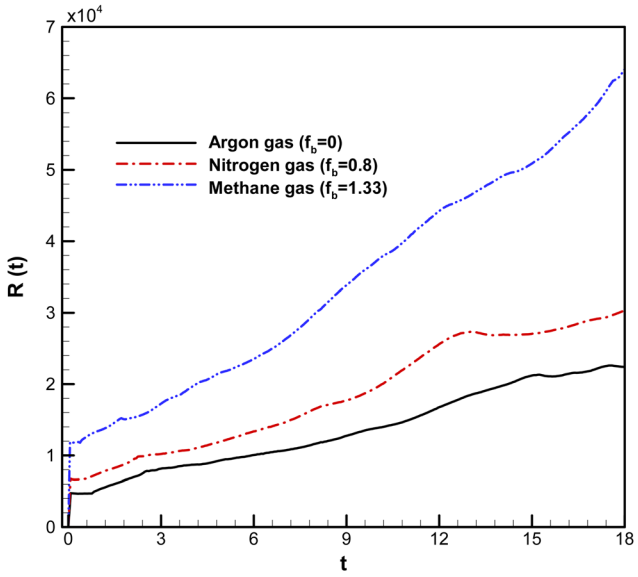

FIG. 16. Effects of diatomic and polyatomic gases on the shock-accelerated cylindrical He bubble: spatially integrated fields of degree of thermal non-equilibrium.

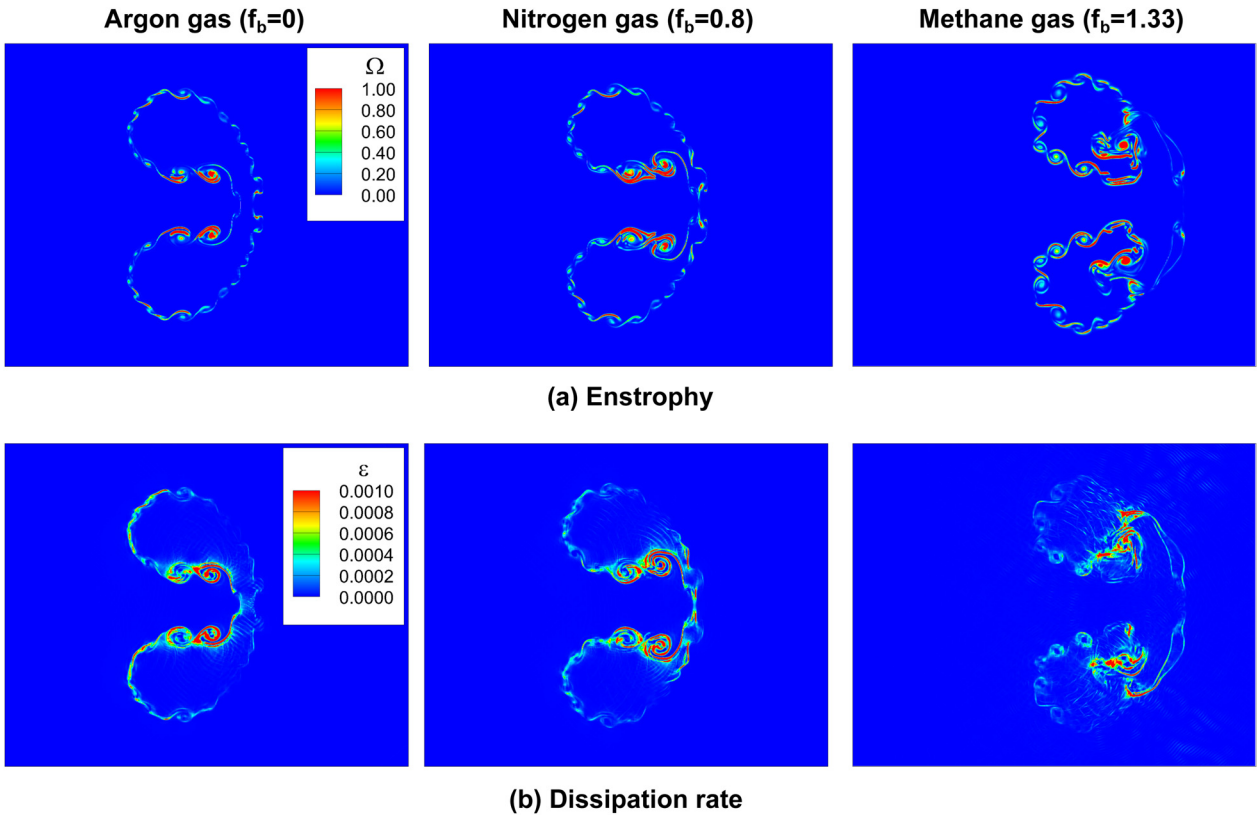

FIG. 17. Effects of diatomic and polyatomic gases on the shock-accelerated cylindrical He bubble: contours of (a) enstrophy (Ω), and (b) dissipation rate (ϵ) in argon gas (left), nitrogen gas (middle), and methane gas (right) at time $t = 12$.

during the interaction are substantially enhanced in diatomic and polyatomic gases. To further explore the effects of diatomic and polyatomic gases on the shock-accelerated cylindrical He bubble, the spatially integrated fields of the enstrophy and dissipation rate are shown in Fig. 17. The enstrophy and dissipation rate during the interaction are substantially higher for diatomic and polyatomic gases than for monatomic gases. Diatomic and polyatomic gases exhibit very similar evolution profiles. Specifically, the enstrophy increases when the IS

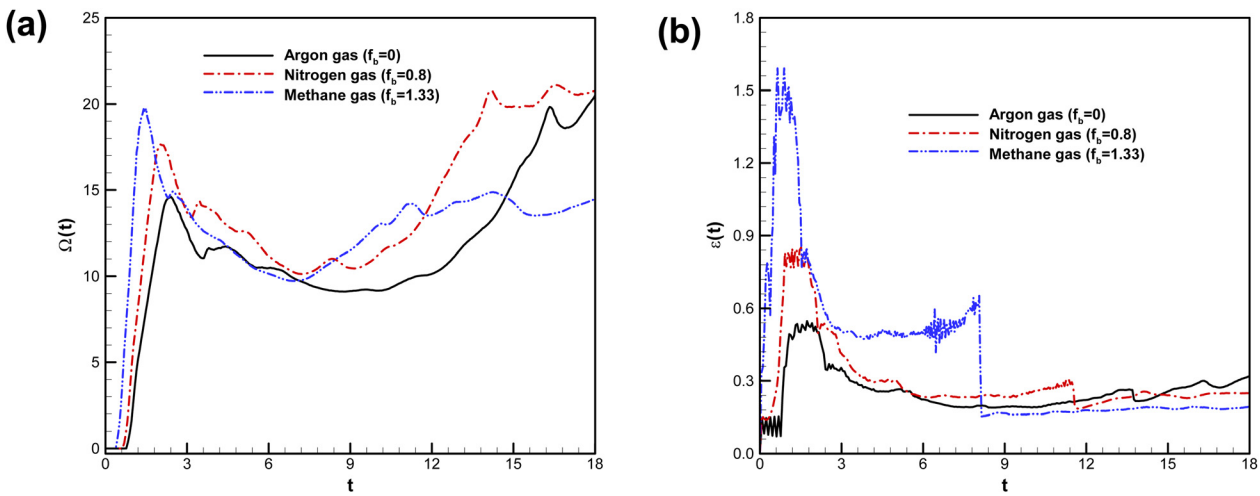

FIG. 18. Effects of diatomic and polyatomic gases on the shock-accelerated cylindrical He bubble: spatially integrated fields of (a) enstrophy (Ω), and (b) dissipation rate (ϵ).

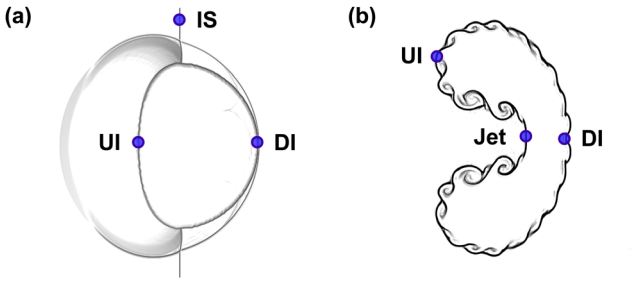

FIG. 19. Schematic diagram with the shock trajectory points during the interaction between the shock and light bubble: (a) early stage of the interaction, (b) a time instant after the shock wave passed through the bubble. Characteristics interface points: incident shock IS; upstream interface UI; downstream interface DI; and jet-head.

and RS waves impinge on the bubbles. Subsequently, the enhanced vorticity promotes the mixing of gases inside and outside the gas bubble and thus accelerates the transfer and consumption of vorticity energy, which gradually weakens the enstrophy intensity in the bubble region, as shown in Fig. 18(a). This phenomenon can also be observed in the time evolution of the dissipation rate, as shown in Fig. 18(b). Moreover, nonmonotonic trends appear in the enstrophy and dissipation rate throughout the interaction process.

5. Shock trajectories and interface features

To investigate the effects of diatomic and polyatomic gases on the shock-accelerated cylindrical He bubble, a quantitative analysis of the shock trajectories and interface features is now presented. Figure 19

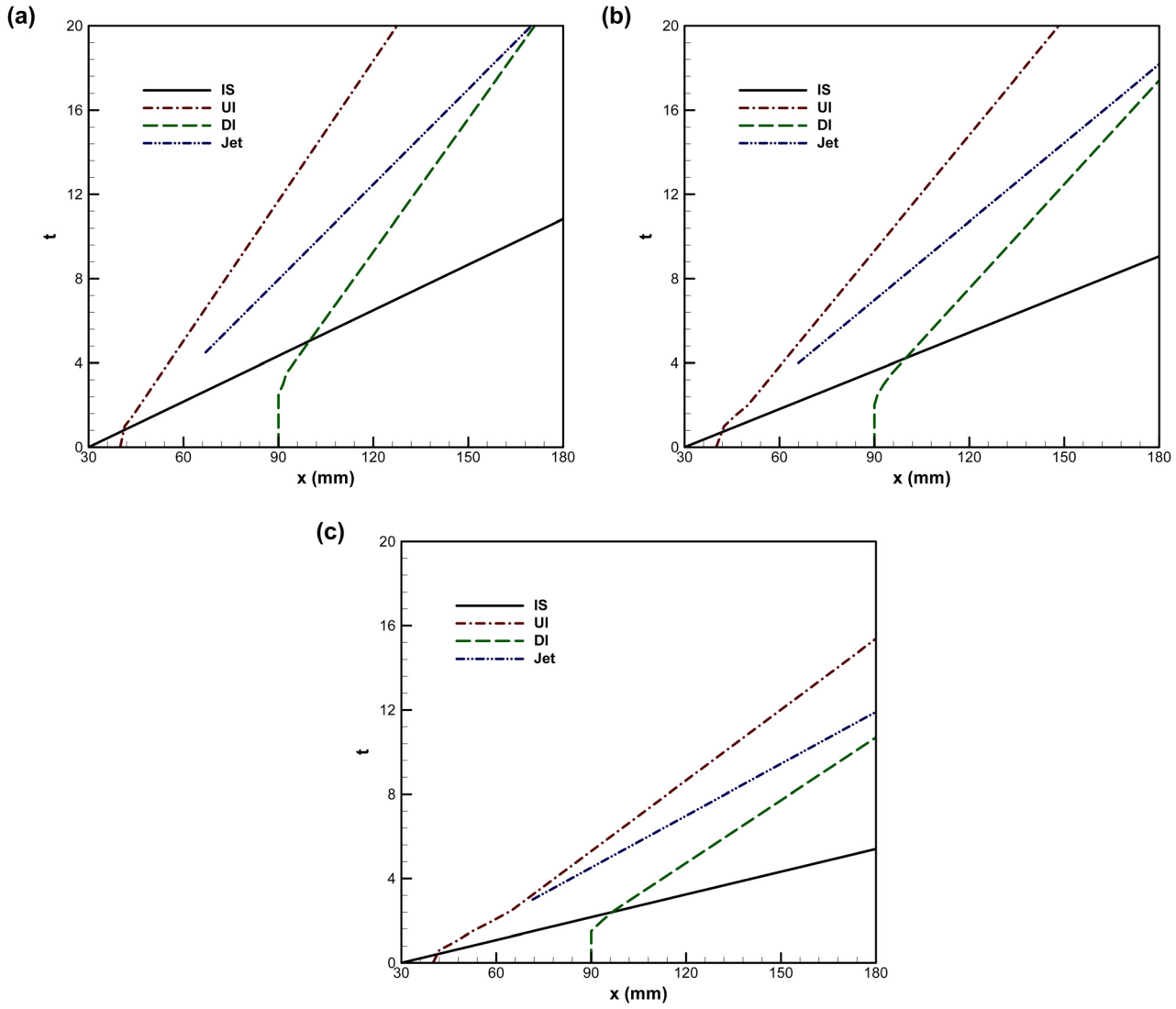

FIG. 20. Effects of diatomic and polyatomic gases on the shock-accelerated cylindrical He bubble: shock trajectories (IS, UI, DI, and Jet) for the computed bubble in (a) argon gas ($f_b = 0$), (b) nitrogen gas ($f_b = 0.8$), and (c) methane gas ($f_b = 1.33$).

shows a schematic diagram of the shock trajectory points (incident shock IS; upstream interface UI; downstream interface DI; and jet-head) at an early stage of the interaction and after the shock wave has passed through the bubble. Figure 20 illustrates the effects of diatomic and polyatomic gases on the shock trajectory points (IS, UI, DI, and jet) indicated in Fig. 19. It can be observed from these figures that the fastest IS wave occurs in methane, while the slowest wave is formed in argon.

Figure 21 illustrates the effects of diatomic and polyatomic gases on the temporal variations of the interfacial characteristic scales (i.e., the length and height of the evolving interface) for the computed cylindrical He bubble. The length and height of the evolving interface are defined in the figure. Early shock compression rapidly reduces the length of the evolving interface after the incident shock arrives for all ambient gases, as shown in Fig. 21(a). The interface lengths in argon, nitrogen, and methane gases reach a minimum value at around $t = 5$, 4, and 3, respectively. As indicated in Fig. 21(a), the upstream interface becomes flatter at this moment. Later, after the compression phase, the variation of length with time tends to increase due to the enhanced rolled-up vortices, as seen in Fig. 10. However, the growth in the width of the evolving interface gradually decreases and tends to a constant value after $t = 18$, at which time the He jet reaches the downstream interface. When the He jet penetrates through the evolving interface, a vortex pair with a nearly constant distance between the two components gradually develops. Figure 21(b) shows that methane gives the maximum interface height, while argon produces the minimum interface height.

C. Effects of bulk viscosity on shock-accelerated cylindrical He bubble

The bulk viscosity plays a vital role in the nonequilibrium effects of diatomic and polyatomic gases. To investigate the effect of bulk viscosity on a shock-accelerated cylindrical He bubble, the contours of the degree of thermal nonequilibrium (R) and the dissipation rate (ϵ) for both nitrogen and methane gases at $t = 13$ are plotted in Fig. 22. In these plots, the upper part corresponds to the numerical simulation without the bulk viscosity ratio, that is, $f_b = 0$, whereas the lower part corresponds to the same simulation with the bulk viscosity ratio. The bulk viscosity has a non-negligible effect on the flow morphology of the shock-accelerated cylindrical He bubble, particularly in terms of the creation of the rolled-up vortices in the absence and presence of the excess normal stress, i.e., $\Delta = 0$ and $\Delta \neq 0$, as shown in Figs. 22(a) and 22(b). Note that the excess normal stress is proportional to f_b ($\Delta = -f_b \mu \nabla \cdot \mathbf{u}$). Interestingly, the deformed bubble interface is more pronounced with $f_b \neq 0$ than when $f_b = 0$. Moreover, there is a significant increase in the degree of thermal nonequilibrium and the dissipation rate with a nonzero f_b value in both nitrogen and methane gases, as seen in Figs. 22(a) and 22(b).

The nonequilibrium effect of the bulk viscosity can also be seen in the spatially integrated fields of physical quantities, that is, degree of thermal nonequilibrium and dissipation rate during the interaction process, as shown in Fig. 23. From the evolution profiles, it is clear that a nonzero bulk viscosity significantly influences the flow morphology, resulting in nonequilibrium phenomena in diatomic and polyatomic gases.

V. CONCLUDING REMARKS

Shock-accelerated bubbles have long been an intriguing topic for understanding the fundamental physics of turbulence generation and mixing caused by the Richtmyer–Meshkov (RM) instability. This study has investigated the impacts of bulk viscosity on the flow morphology of a shock-accelerated cylindrical light bubble in diatomic and polyatomic gases. A two-dimensional system of unsteady physical conservation laws for diatomic and polyatomic gases was rigorously derived from the Boltzmann–Curtiss kinetic equations and solved by employing an explicit mixed-type modal discontinuous Galerkin method with uniform meshes. A new complete viscous compressible vorticity transport equation including the bulk viscosity was also derived. The computational model was validated against existing

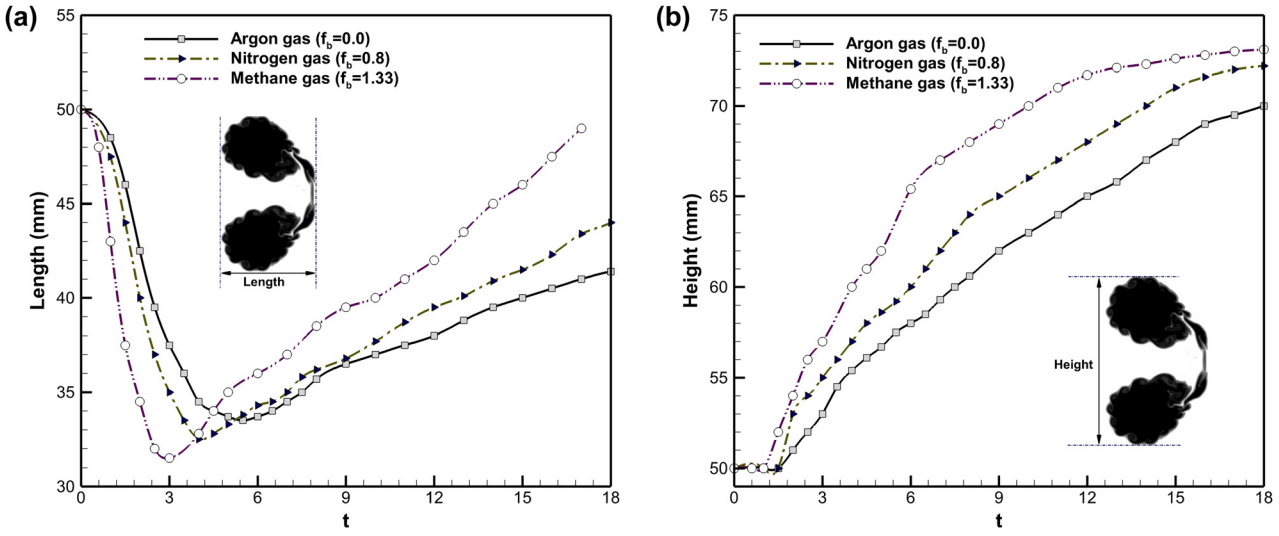

FIG. 21. Effects of diatomic and polyatomic gases on the shock-accelerated cylindrical He bubble: temporal variations of the interfacial characteristic scales—(a) the length, and (b) the height—of the evolving interface for the computed bubble. The definitions of the length and the height of the evolving interface are inserted.

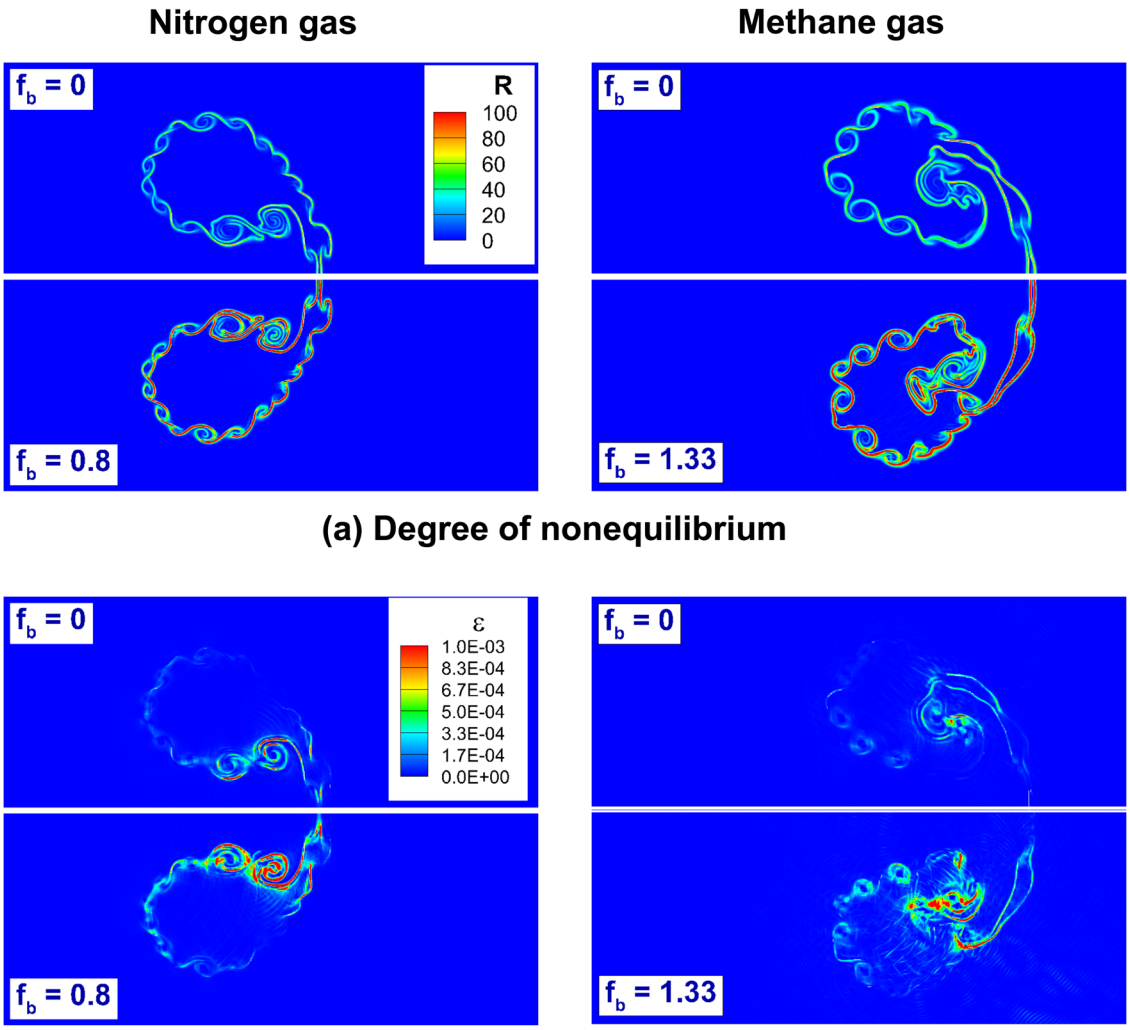

FIG. 22. Effects of bulk viscosity on the shock-accelerated cylindrical He bubble: contours of (a) degree of nonequilibrium, and (b) dissipation rate for nitrogen (left), and methane gases (right) at time instant $t = 13$.

experimental and numerical data for the shock-accelerated cylindrical light bubble problems.

The numerical results reveal that the effects of bulk viscosity associated with the viscous excess normal stress, including different physical properties of diatomic and polyatomic gases, play a vital role in describing the RM instability during the interaction between a planar shock wave and a light bubble. Other physical properties, such as the density and specific heat ratio, may also have contributed to the current observations. The effects of diatomic and polyatomic gases result in a significant change in the flow morphology, including complex wave patterns, vortex creation, vorticity generation, and bubble deformation. In contrast to monatomic gases, diatomic and polyatomic gases generate larger rolled-up vortex chains, different kinds of inward jet formation, and large mixing zones with strong and large-scale expansion.

The effects of diatomic and polyatomic gases have been studied in depth through the vorticity generation, degree of nonequilibrium, enstrophy, and dissipation rate. Interestingly, both vorticity and the degree of nonequilibrium play an important role in describing the essential features of the shock-accelerated bubble. In addition, the time variations of the shock trajectories and interface features were investigated. Finally, the effects of bulk viscosity, which is directly related to the rotational mode, were investigated. The numerical results have demonstrated that the bulk viscosity is pivotal in generating the nonequilibrium effects observed in diatomic and polyatomic gases, and substantially changes the flow fields of the bubble after interaction with the IS wave. Increasing the bulk viscosity ratio significantly enhances the degree of nonequilibrium and the dissipation rate.

The primary focus of this research was to investigate the impacts of bulk viscosity with the different physical properties of diatomic and

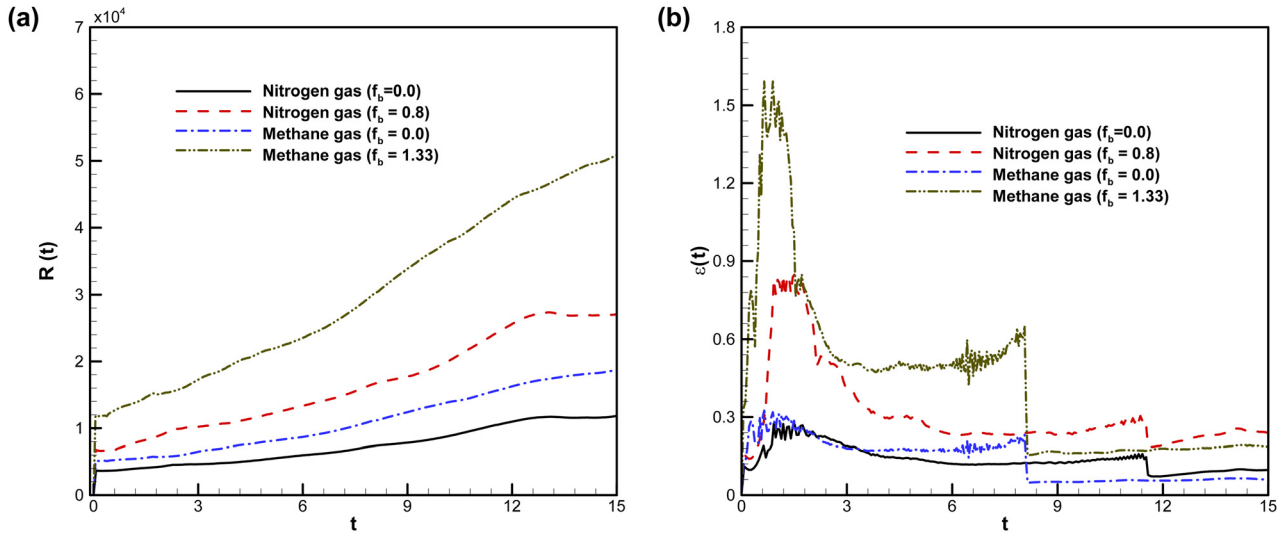

FIG. 23. Effects of bulk viscosity on the shock-accelerated cylindrical He bubble: spatially integrated fields of (a) degree of nonequilibrium, (b) dissipation rate in nitrogen, and methane gases.

polyatomic gases on a shock-accelerated cylindrical light bubble with a single-component gas model. However, the vibrational mode of the gases and the chemical reaction kinetics, including the bulk viscosity beyond Stokes' hypothesis, play an essential role in determining the nonequilibrium effects of diatomic and polyatomic gases in compressible multicomponent gas flows. It is also expected that the nonequilibrium behavior will significantly affect the development of the RM instability in compressible multicomponent gas flows. In this context, the present work will be expanded in the future to investigate the effects of the vibrational mode and chemical reaction kinetics, including the bulk viscosity, on the flow dynamics in shock-accelerated polygonal bubbles with different interface shapes.

ACKNOWLEDGMENTS

S.S. and M.B. acknowledge the support provided by the Nanyang Technological University Singapore, through the NAP-SUG grant. R.S.M. derived a new complete viscous compressible vorticity transport equation summarized in the Appendix. R.S.M. acknowledges the support from the National Research Foundation of Korea funded by the Ministry of Science and ICT (NRF 2017-R1A5A1015311 and NRF 2017-R1A2B2007634), South Korea.

APPENDIX: DERIVATION OF COMPLETE VISCOUS COMPRESSIBLE VORTICITY TRANSPORT EQUATION INCLUDING THE BULK VISCOSITY

We consider flows of diatomic and polyatomic gases with considerable variations in temperature in the flow fields. As we are dealing with diatomic and polyatomic gases, we abandon Stokes' hypothesis, resulting in the following compressible version of the momentum equation with varying transport coefficients:

$$\frac{\partial(\rho\mathbf{u})}{\partial t}+\nabla\cdot(\rho\mathbf{u}\mathbf{u}+p\mathbf{I})-\nabla\cdot\left(2\mu[\nabla\mathbf{u}]^{(2)}\right)-\nabla\cdot(\mu_b(\nabla\cdot\mathbf{u})\mathbf{I})=0. \tag{A1}$$

The corresponding viscous compressible vorticity transport equation, after lengthy derivation, can be summarized as

$$\begin{aligned}\frac{D\boldsymbol{\omega}}{Dt}&=(\boldsymbol{\omega}\cdot\nabla)\mathbf{u}-\boldsymbol{\omega}(\nabla\cdot\mathbf{u})+\frac{\mu}{\rho}\nabla^2\boldsymbol{\omega}\\&+\frac{1}{\rho^2}\nabla\rho\times\nabla p-\frac{\mu}{\rho^2}\nabla\rho\times\nabla^2\mathbf{u}-\left(\frac{1}{3}+f_b\right)\frac{\mu}{\rho^2}\nabla\rho\times\nabla(\nabla\cdot\mathbf{u})\\&+\frac{1}{\rho}(\nabla\mu\cdot\nabla)\boldsymbol{\omega}+\frac{1}{\rho}(\boldsymbol{\omega}\cdot\nabla)\nabla\mu-\frac{\boldsymbol{\omega}}{\rho}\nabla^2\mu+\frac{1}{\rho}\nabla\mu\times\nabla^2\mathbf{u}\\&+\frac{2}{\rho}\nabla(\nabla\mu\cdot\nabla)\times\mathbf{u}-\frac{1}{\rho^2}\nabla\rho\times(\nabla\mu\times\boldsymbol{\omega})-\frac{2}{\rho^2}\nabla\rho\\&\times(\nabla\mu\cdot\nabla)\mathbf{u}+\left(\frac{2}{3}-f_b\right)\frac{(\nabla\cdot\mathbf{u})}{\rho^2}\nabla\rho\times\nabla\mu+\frac{1}{\rho}\nabla\mu\times\nabla(\nabla\cdot\mathbf{u}).\end{aligned} \tag{A2}$$

We believe this equation to be new. (In the previous literature, only the first four of the fifteen terms on the right-hand side were retained.) The second line is related to $\nabla\rho$, the third line includes terms in $\nabla\mu$, and the fourth line has terms in $\nabla\rho$ [or $\nabla(\nabla\cdot\mathbf{u})$] and $\nabla\mu$. There are two terms associated with the bulk viscosity, $-f_b[\mu\nabla\rho\times\nabla(\nabla\cdot\mathbf{u})+(\nabla\cdot\mathbf{u})\nabla\rho\times\nabla\mu]/\rho^2$.

The detailed derivation of Eq. (A2) from Eq. (A1) can be summarized as follows. The conservation law of momentum can be rewritten as

$$\begin{aligned}&\frac{\partial\rho}{\partial t}=-(\mathbf{u}\cdot\nabla)\mathbf{u}-\frac{1}{\rho}\nabla p+\frac{1}{\rho}\nabla\cdot\left(2\mu[\nabla\mathbf{u}]^{(2)}+\mu_b(\nabla\cdot\mathbf{u})\mathbf{I}\right),\\\text{Or}\quad&\frac{\partial\rho}{\partial t}=-(\mathbf{u}\cdot\nabla)\mathbf{u}-\frac{1}{\rho}\nabla p+\frac{1}{\rho}\nabla\cdot\left[\mu\left(2[\nabla\mathbf{u}]^{(2)}+f_b(\nabla\cdot\mathbf{u})\mathbf{I}\right)\right].\end{aligned} \tag{A3}$$

Using the relation

$$2[\nabla \mathbf{u}]^{(2)} \equiv (\nabla \mathbf{u}^T + \nabla \mathbf{u}) - \frac{2}{3}(\nabla \cdot \mathbf{u})\mathbf{I} = 2\nabla \mathbf{u}^T + \text{tensor}(\boldsymbol{\omega}) - \frac{2}{3}(\nabla \cdot \mathbf{u})\mathbf{I}, \tag{A4}$$

we can show that

$$\begin{aligned}
&\frac{1}{\rho}\nabla \cdot \left(2\mu[\nabla \mathbf{u}]^{(2)}\right) \\
&= \frac{1}{\rho}\nabla \cdot \left[2\mu\nabla \mathbf{u}^T + \mu\,\text{tensor}(\boldsymbol{\omega}) - \frac{2}{3}\mu(\nabla \cdot \mathbf{u})\mathbf{I}\right] \\
&= \frac{1}{\rho}\left[2\nabla \cdot (\mu\nabla \mathbf{u}^T) + \nabla \cdot (\mu\,\text{tensor}(\boldsymbol{\omega})) - \frac{2}{3}\nabla(\mu(\nabla \cdot \mathbf{u}))\right] \\
&= \frac{1}{\rho}\left[2\nabla \cdot (\mu\nabla \mathbf{u}^T) + \nabla \times (\mu\boldsymbol{\omega}) - \frac{2}{3}\nabla(\mu(\nabla \cdot \mathbf{u}))\right], \\
&\frac{1}{\rho}\nabla \cdot (f_b\mu(\nabla \cdot \mathbf{u})\mathbf{I}) = \frac{f_b}{\rho}\nabla(\mu(\nabla \cdot \mathbf{u})),
\end{aligned} \tag{A5}$$

and

$$\frac{\partial \mathbf{u}}{\partial t} = -(\mathbf{u} \cdot \nabla)\mathbf{u} - \frac{1}{\rho}\nabla p + \frac{2}{\rho}\nabla \cdot (\mu\nabla \mathbf{u}^T) + \frac{1}{\rho}\nabla \times (\mu\boldsymbol{\omega}) + \frac{1}{\rho}\left(f_b - \frac{2}{3}\right)\nabla(\mu(\nabla \cdot \mathbf{u})). \tag{A6}$$

Using the following identities for a scalar ϕ, vector $\mathbf{A}$, and tensor $\mathbf{T}$:

$$\begin{aligned}
\nabla \cdot (\phi\mathbf{A}) &= \phi\nabla \cdot \mathbf{A} + \mathbf{A} \cdot \nabla\phi, \\
\nabla \cdot (\phi\mathbf{T}) &= \phi\nabla \cdot \mathbf{T} + \mathbf{T} \cdot \nabla\phi, \\
\nabla \times (\phi\mathbf{A}) &= \phi\nabla \times \mathbf{A} + \nabla\phi \times \mathbf{A}, \\
\nabla \times (\nabla \times \mathbf{A}) &= \nabla(\nabla \cdot \mathbf{A}) - \nabla^2\mathbf{A},
\end{aligned}$$

we obtain

$$\begin{aligned}
\nabla \cdot (\mu\nabla \mathbf{u}^T) &= (\nabla\mu \cdot \nabla)\mathbf{u} + \mu\nabla^2\mathbf{u}, \\
\nabla \times (\mu\boldsymbol{\omega}) &= \mu\nabla \times \boldsymbol{\omega} + \nabla\mu \times \boldsymbol{\omega} = \mu\nabla(\nabla \cdot \mathbf{u}) - \mu\nabla^2\mathbf{u} + \nabla\mu \times \boldsymbol{\omega}.
\end{aligned} \tag{A7}$$

Then, Eq. (A6) can be rewritten as

$$\frac{\partial \mathbf{u}}{\partial t} = -(\mathbf{u} \cdot \nabla)\mathbf{u} - \frac{1}{\rho}\nabla p + \frac{\mu}{\rho}\nabla^2\mathbf{u} + \frac{2}{\rho}(\nabla\mu \cdot \nabla)\mathbf{u} + \frac{1}{\rho}(\nabla\mu \times \boldsymbol{\omega}) + \frac{\mu}{\rho}\nabla(\nabla \cdot \mathbf{u}) + \frac{1}{\rho}\left(f_b - \frac{2}{3}\right)\nabla(\mu(\nabla \cdot \mathbf{u})). \tag{A8}$$

Finally, we can derive the viscous compressible vorticity transport equation in Eq. (A2) by applying $\nabla\times$ to each term.

First term

$$\nabla \times \left(\frac{\partial \mathbf{u}}{\partial t}\right) = \frac{\partial(\nabla \times \mathbf{u})}{\partial t} = \frac{\partial \boldsymbol{\omega}}{\partial t}.$$

Second term

$$\begin{aligned}
-\nabla \times [(\mathbf{u} \cdot \nabla)\mathbf{u}] &= -\nabla \times \left[\nabla\left(\frac{\mathbf{u} \cdot \mathbf{u}}{2}\right) + \boldsymbol{\omega} \times \mathbf{u}\right] = -\nabla \times (\boldsymbol{\omega} \times \mathbf{u}) \\
&= \nabla \cdot (\boldsymbol{\omega}\mathbf{u} - \mathbf{u}\boldsymbol{\omega}) = (\boldsymbol{\omega} \cdot \nabla)\mathbf{u} - (\mathbf{u} \cdot \nabla)\boldsymbol{\omega} - \boldsymbol{\omega}(\nabla \cdot \mathbf{u}),
\end{aligned}$$

where we have used the following identities for a scalar ϕ and vectors $\mathbf{A}$, $\mathbf{B}$:

$$\begin{aligned}
\nabla \times \nabla\phi &= \nabla \cdot (\nabla \times \mathbf{A}) = 0, \\
\nabla \times (\mathbf{A} \times \mathbf{B}) &= \nabla \cdot (\mathbf{BA} - \mathbf{AB}).
\end{aligned}$$

Third term

$$-\nabla \times \left(\frac{1}{\rho}\nabla p\right) = \frac{1}{\rho^2}\nabla\rho \times \nabla p - \frac{1}{\rho}\nabla \times \nabla p = \frac{1}{\rho^2}\nabla\rho \times \nabla p.$$

Fourth term

$$\begin{aligned}
\nabla \times \left(\frac{\mu}{\rho}\nabla^2\mathbf{u}\right) &= \nabla\left(\frac{\mu}{\rho}\right) \times \nabla^2\mathbf{u} + \frac{\mu}{\rho}\nabla \times (\nabla^2\mathbf{u}) \\
&= \nabla\left(\frac{\mu}{\rho}\right) \times \nabla^2\mathbf{u} - \frac{\mu}{\rho} \times (\nabla \times \boldsymbol{\omega}) \\
&= \nabla\left(\frac{\mu}{\rho}\right) \times \nabla^2\mathbf{u} + \frac{\mu}{\rho}\nabla^2\boldsymbol{\omega} \\
&= \frac{1}{\rho}\nabla\mu \times \nabla^2\mathbf{u} - \frac{\mu}{\rho^2}\nabla\rho \times \nabla^2\mathbf{u} + \frac{\mu}{\rho}\nabla^2\boldsymbol{\omega}.
\end{aligned}$$

Fifth term

$$\nabla \times \left[\frac{2}{\rho}(\nabla\mu \cdot \nabla)\mathbf{u}\right] = -\frac{2}{\rho^2}\nabla\rho \times (\nabla\mu \cdot \nabla)\mathbf{u} + \frac{2}{\rho}(\nabla\mu \cdot \nabla)\boldsymbol{\omega} + \frac{2}{\rho}\nabla(\nabla\mu \cdot \nabla) \times \mathbf{u}.$$

Sixth term

$$\begin{aligned}
\nabla \times \left(\frac{1}{\rho}\nabla\mu \times \boldsymbol{\omega}\right) &= -\frac{1}{\rho^2}\nabla\rho \times (\nabla\mu \times \boldsymbol{\omega}) + \frac{1}{\rho}\nabla \times (\nabla\mu \times \boldsymbol{\omega}) \\
&= -\frac{1}{\rho^2}\nabla\rho \times (\nabla\mu \times \boldsymbol{\omega}) + \frac{1}{\rho}(\boldsymbol{\omega} \cdot \nabla)\nabla\mu \\
&\quad - \frac{1}{\rho}(\nabla\mu \cdot \nabla)\boldsymbol{\omega} - \frac{\boldsymbol{\omega}}{\rho}\nabla^2\mu.
\end{aligned}$$

Seventh term

$$\begin{aligned}
\nabla \times \left[\frac{\mu}{\rho}\nabla(\nabla \cdot \mathbf{u})\right] &= \nabla\left(\frac{\mu}{\rho}\right) \times \nabla(\nabla \cdot \mathbf{u}) \\
&= \frac{1}{\rho}\nabla\mu \times \nabla(\nabla \cdot \mathbf{u}) - \frac{\mu}{\rho^2}\nabla\rho \times \nabla(\nabla \cdot \mathbf{u}).
\end{aligned}$$

Eighth term

$$\begin{aligned}
&\nabla \times \left[\frac{1}{\rho}\left(f_b - \frac{2}{3}\right)\nabla(\mu(\nabla \cdot \mathbf{u}))\right] \\
&= \left(f_b - \frac{2}{3}\right)\nabla\left(\frac{1}{\rho}\right) \times \nabla(\mu(\nabla \cdot \mathbf{u})) \\
&= -\left(f_b - \frac{2}{3}\right)\left[\frac{(\nabla \cdot \mathbf{u})}{\rho^2}\nabla\rho \times \nabla\mu + \frac{\mu}{\rho^2}\nabla\rho \times \nabla(\nabla \cdot \mathbf{u})\right].
\end{aligned}$$

DATA AVAILABILITY

The data that support the findings of this study are available from the corresponding author upon reasonable request.

REFERENCES

[1]R. D. Richtmyer, "Taylor instability in shock acceleration of compressible fluids," Commun. Pure Appl. Math. **13**, 297–319 (1960).
[2]E. Meshkov, "Instability of the interface of two gases accelerated by a shock wave," Fluid Dyn. **4**, 101–104 (1969).
[3]J. D. Lindl, R. L. McCrory, and E. M. Campbell, "Progress toward ignition and burn propagation in inertial confinement fusion," Phys. Today **45**(9), 32–40 (1992).
[4]W. D. Arnett, J. N. Bahcall, R. P. Kirshner *et al.*, "Supernova 1987A," Annu. Rev. Astron. Astrophys. **27**, 629–700 (1989).
[5]A. R. Jamaluddin, G. J. Ball, and T. G. Leighton, "Shock/bubble interaction near a rigid boundary in shock wave lithotripsy," in *24th International Symposium on Shock Waves* (Springer, 2005), pp. 1211–1216.
[6]F. E. Marble, G. J. Hendricks, and E. E. Zukoski, "Progress toward shock enhancement of supersonic combustion processes," in *Turbulent Reactive Flows* (Springer, 1989).
[7]Y. Yang, T. Kubota, and E. E. Zukoski, "Applications of shock-induced mixing to supersonic combustion," AIAA J. **31**, 854–862 (1993).
[8]D. Arnett, "The role of mixing in astrophysics," Astrophys. J., Suppl. Ser. **127**, 213 (2000).
[9]A. M. Goodbody, *Cartesian Tensors: With Applications to Mechanics, Fluid Mechanics and Elasticity* (Ellis Horwood Ltd., Chichester, England, 1982).
[10]S. A. Kinnas, "VIScous vorticity equation (VISVE) for turbulent 2-D flows with variable density and viscosity," J. Mar. Sci. Eng. **8**(3), 191 (2020).
[11]G. H. Markstein, "A shock-tube study of flame front-pressure wave interaction," Symp. (Int.) Combust. **6**, 387–398 (1957).
[12]G. Rudinger and L. M. Somers, "Behavior of small regions of different gases carried in accelerated gas flows," J. Fluid Mech. **7**, 161–176 (1960).
[13]J. F. Haas and B. Sturtevant, "Interaction of weak shock waves with cylindrical and spherical gas inhomogeneities," J. Fluid Mech. **181**, 41–76 (1987).
[14]J. W. Jacobs, "Shock-induced mixing of a light-gas cylinder," J. Fluid Mech. **234**, 629–649 (1992).
[15]J. W. Jacobs, "The dynamics of shock accelerated light and heavy gas cylinders," Phys. Fluids **5**, 2239–2247 (1993).
[16]G. Layes, G. Jourdan, and L. Houas, "Experimental investigation of the shock wave interaction with a spherical gas inhomogeneity," Phys. Fluids **17**, 028103 (2005).
[17]G. Layes, G. Jourdan, and L. Houas, "Experimental study on a plane shock wave accelerating a gas bubble," Phys. Fluids **21**, 074102 (2009).
[18]D. Ranjan, J. H. J. Niederhaus, B. Motl, M. H. Anderson, J. Oakley, and R. Bonazza, "Experimental investigation of primary and secondary features in high-Mach-number shock-bubble interaction," Phys. Rev. Lett. **98**, 024502 (2007).
[19]D. Ranjan, J. H. J. Niederhaus, J. G. Oakley, M. H. Anderson, R. Bonazza, and J. A. Greenough, "Shock-bubble interactions: Features of divergent shock refraction geometry observed in experiments and simulations," Phys. Fluids **20**, 036101 (2008).
[20]J. J. Quirk and S. Karni, "On the dynamics of a shock–bubble interaction," J. Fluid Mech. **318**, 129–163 (1996).
[21]N. J. Zabusky and S. M. Zeng, "Shock cavity implosion morphologies and vortical projectile generation in axisymmetric shock-spherical fast/slow bubble interactions," J. Fluid Mech. **362**, 327–346 (1998).
[22]A. Bagabir and D. Drikakis, "Mach number effects on shock-bubble interaction," Shock Waves **11**, 209–218 (2001).
[23]J. J. Niederhaus, J. A. Greenough, J. G. Oakley, D. Ranjan, M. H. Anderson, and R. Bonazza, "A computational parameter study for the three-dimensional shock-bubble interaction," J. Fluid Mech. **594**, 85 (2008).
[24]Y. J. Zhu, G. Dong, B. C. Fan, and Y. X. Liu, "Formation and evolution of vortex rings induced by interactions between shock waves and a low-density bubble," Shock Waves **22**, 495 (2012).
[25]Y. J. Zhu, L. Yu, J. F. Pan, Z. H. Pan, and P. G. Zhang, "Jet formation of SF6 bubble induced by incident and reflected shock waves," Phys. Fluids **29**, 126105 (2017).
[26]Y. J. Zhu, Z. W. Yang, K. H. Luo, J. F. Pan, and Z. H. Pan, "Numerical investigation of planar shock wave impinging on spherical gas bubble with different densities," Phys. Fluids **31**, 056101 (2019).
[27]B. Rybakin and V. Goryachev, "The supersonic shock wave interaction with low-density gas bubble," Acta Astronaut. **94**(2), 749–753 (2014).
[28]B. P. Rybakin, V. B. Betelin, V. R. Dushin, E. V. Mikhalchenko, S. G. Moiseenko, L. I. Stamov, and V. V. Tyurenkova, "Model of turbulent destruction of molecular clouds," Acta Astronaut. **119**, 131–136 (2016).
[29]B. P. Rybakin, V. B. Betelin, N. N. Smirnov, S. G. Moiseenko, and L. I. Stamov, "3D numerical simulation of molecular clouds collision process," J. Phys.: Conf. Ser. **1103**, 012007 (2018).
[30]B. P. Rybakin, V. D. Goryachev, L. I. Stamov, E. V. Mikhalchenko, V. V. Tyurenkova, M. N. Smirnova, A. A. Shamina, E. I. Kolenkina, and D. A. Pestov, "Modeling the formation of dense clumps during molecular clouds collision," Acta Astronaut. **170**, 586–591 (2020).
[31]Z. Wang, B. Yu, H. Chen, B. Zhang, and H. Liu, "Scaling vortex breakdown mechanism based on viscous effect in shock cylindrical bubble interaction," Phys. Fluids **30**, 126103 (2018).
[32]S. Singh, "Role of Atwood number on flow morphology of a planar shock-accelerated square bubble: A numerical study," Phys. Fluids **32**, 126112 (2020).
[33]G. G. Stokes, "On the theories of the internal friction of fluids in motion, and of the equilibrium and motion of elastic fluids," Trans. Cambridge Philos. Soc. **8**, 287–305 (1845).
[34]G. Emanuel, "Bulk viscosity of a dilute polyatomic gas," Phys. Fluids A **2**, 2252–2254 (1990).
[35]G. Emanuel, "Bulk viscosity in the Navier–Stokes equations," Int. J. Eng. Sci. **36**, 1313–1323 (1998).
[36]B. C. Eu and Y. G. Ohr, "Generalized hydrodynamics, bulk viscosity, and sound wave absorption and dispersion in dilute rigid molecular gases," Phys. Fluids **13**, 744 (2001).
[37]N. Carlevaro and G. Montani, "Bulk viscosity effects on the early universe stability," Mod. Phys. Lett. A **20**, 1729–1739 (2005).
[38]G. Billet, V. Giovangigli, and G. D. Gassowski, "Impact of volume viscosity on a shock–hydrogen-bubble interaction," Combust. Theory Modell. **12**, 221–248 (2008).
[39]M. S. Cramer, "Numerical estimates for the bulk viscosity of ideal gases," Phys. Fluids **24**, 066102 (2012).
[40]Y. Zhu, C. Zhang, X. Chen, H. Yuan, J. Wu, S. Chen, C. Lee, and M. Gad-El-Hak, "Transition in hypersonic boundary layers: Role of dilatational waves," AIAA J. **54**, 3039–3049 (2016).
[41]F. Bahmani and M. S. Cramer, "Suppression of shock-induced separation in fluids having large bulk viscosities," J. Fluid Mech. **756**, 1–10 (2014).
[42]S. Pan and E. Johnsen, "The role of bulk viscosity on the decay of compressible, homogeneous, isotropic turbulence," J. Fluid Mech. **833**, 717–744 (2017).
[43]R. S. Myong, "A generalized hydrodynamic computational model for rarefied and microscale diatomic gas flows," J. Comput. Phys. **195**, 655 (2004).
[44]S. Singh and R. S. Myong, "A computational study of bulk viscosity effects on shock-vortex interaction using discontinuous Galerkin method," J. Comput. Fluids Eng. **22**, 86–95 (2017).
[45]S. Singh, A. Karchani, and R. S. Myong, "Non-equilibrium effects of diatomic and polyatomic gases on the shock-vortex interaction based on the second-order constitutive model of the Boltzmann–Curtiss equation," Phys. Fluids **30**, 016109 (2018).
[46]S. Singh, "Development of a 3D discontinuous Galerkin method for the second-order Boltzmann–Curtiss based hydrodynamic models of diatomic and polyatomic gases," Ph.D. thesis (Gyeongsang National University, South Korea, 2018).
[47]B. Sharma and R. Kumar, "Estimation of bulk viscosity of dilute gases using a non-equilibrium molecular dynamics approach," Phys. Rev. E **100**, 013309 (2019).
[48]S. Singh, A. Karchani, K. Sharma, and R. S. Myong, "Topology of the second-order constitutive model based on the Boltzmann–Curtiss kinetic equation for diatomic and polyatomic gases," Phys. Fluids **32**, 026104 (2020).
[49]S. Singh and M. Battiato, "Behavior of a shock accelerated heavy cylindrical bubble under nonequilibrium conditions of diatomic and polyatomic gases," Phys. Rev. Fluids **6**, 044001 (2021).
[50]R. S. Myong, "Thermodynamically consistent hydrodynamic computational models for high-Knudsen-number gas flows," Phys. Fluids **11**, 2788 (1999).
[51]N. T. P. Le, H. Xiao, and R. S. Myong, "A triangular discontinuous Galerkin method for non-Newtonian implicit constitutive models of rarefied and microscale gases," J. Comput. Phys. **273**, 160 (2014).

[52]T. K. Mankodi and R. S. Myong, "Boltzmann-based second-order constitutive models of diatomic and polyatomic gases including the vibrational mode," Phys. Fluids **32**, 126109 (2020).
[53]J. Giordano and Y. Burtschell, "Richtmyer–Meshkov instability induced by shock-bubble interaction: Numerical and analytical studies with experimental validation," Phys. Fluids **18**, 028603 (2006).
[54]S. K. Shankar, S. Kawai, and S. K. Lele, "Two-dimensional viscous flow simulation of a shock accelerated heavy gas cylinder," Phys. Fluids **23**, 024102 (2011).
[55]J. M. Picone and J. P. Boris, "Vorticity generation by shock propagation through bubbles in a gas," J. Fluid Mech. **189**, 23–51 (1988).
[56]R. Samtaney and N. J. Zabusky, "Circulation deposition on shock-accelerated planar and curved density-stratified interfaces: Models and scaling laws," J. Fluid Mech. **269**, 45–78 (1994).
[57]M. Latini and O. Schilling, "A comparison of two-and three-dimensional single-mode reshocked Richtmyer–Meshkov instability growth," Phys. D **401**, 132201 (2020).
[58]C. F. Curtiss, "The classical Boltzmann equation of a gas of diatomic molecules," J. Chem. Phys. **75**, 376–378 (1981).
[59]S. Chapman and T. G. Cowling, *The Mathematical Theory of Non-Uniform Gases* (Cambridge University Press, Cambridge, 1970).
[60]C. H. Kruger and W. Vincenti, *Introduction to Physical Gas Dynamics* (John Wiley and Sons, 1965).
[61]J. G. Parker, "Rotational and vibrational relaxation in diatomic gases," Phys. Fluids **2**, 449 (1959).
[62]X. D. Li, Z. M. Hu, and Z. L. Jiang, "Continuum perspective of bulk viscosity in compressible fluids," J. Fluid Mech. **812**, 966–990 (2017).
[63]M. A. Saad, *Compressible Fluid Flow* (Prentice-Hall, 1985).
[64]H. J. Hanley and J. F. Ely, "The viscosity and thermal conductivity coefficients of dilute nitrogen and oxygen," J. Phys. Chem. **2**, 735–756 (1973).
[65]G. D. Billing and L. Wang, "Semiclassical calculations of transport coefficients and rotational relaxation of nitrogen at high temperatures," J. Phys. Chem. **96**, 2572–2575 (1992).
[66]E. Vogel, "Präazisionsmessungen des viskositäatskoeffizienten von stickstoff und den edelgasen zwischen raumtemperatur und 650 K," Ber. Bunsengesellsch. Phys. Chem. **88**, 997–1002 (1984).
[67]P. Kistemaker, A. Tom, and A. D. Vries, "Rotational relaxation numbers for the isotopic molecules of N2 and CO," Physica **48**, 414 (1970).
[68]T. G. Winter and G. L. Hill, "High-temperature ultrasonic measurements of rotational relaxation in hydrogen, deuterium, nitrogen, and oxygen," J. Acoust. Soc. Am. **42**, 848 (1967).
[69]Z. Gu and W. Ubachs, "Temperature-dependent bulk viscosity of nitrogen gas determined from spontaneous Rayleigh–Brillouin scattering," Opt. Lett. **38**, 1110 (2013).
[70]A. Meijer, A. de Wijn, M. Peters, N. Dam, and W. van de Water, "Coherent Rayleigh–Brillouin scattering measurements of bulk viscosity of polar and nonpolar gases," J. Chem. Phys. **133**, 164315 (2010).
[71]G. J. Prangsma, A. H. Alberga, and J. Beenakker, "Ultrasonic determination of the volume viscosity of N2, CO, CH4 and CD4 between 77 and 300 K," Physica **64**, 278 (1973).
[72]L. P. Raj, S. Singh, A. Karchani, and R. S. Myong, "A super-parallel mixed explicit discontinuous Galerkin method for the second-order Boltzmann-based constitutive models of rarefied and microscale gases," Comput. Phys. **157**, 146–163 (2017).
[73]S. Singh and M. Battiato, "Strongly out-of-equilibrium simulations for electron Boltzmann transport equation using explicit modal discontinuous Galerkin method," Int. J. Appl. Comput. Math. **6**, 133 (2020).
[74]S. Singh and M. Battiato, "Effect of strong electric fields on material responses: The Bloch oscillation resonance in high field conductivities," Materials **13**, 1070 (2020).
[75]T. Chourushi, A. Rahimi, S. Singh, and R. S. Myong, "Computational simulations of near-continuum gas flow using Navier–Stokes-Fourier equations with slip and jump conditions based on the modal discontinuous Galerkin method," Adv. Aerodyn. **2**, 8 (2020).
[76]S. Singh and M. Battiato, "An explicit modal discontinuous Galerkin method for Boltzmann transport equation under electronic nonequilibrium conditions," Comput. Fluids **224**, 104972 (2021).
[77]S. Singh, A. Karchani, T. Chourushi, and R. S. Myong, "A three-dimensional modal discontinuous Galerkin method for second-order Boltzmann-Curtiss constitutive models of rarefied and microscale gas flows," J. Comput. Phys. (unpublished) (2021).
[78]B. Cockburn and C. W. Shu, "The local discontinuous Galerkin method for time dependent convection-diffusion systems," SIAM J. Numer. Anal. **35**, 2440–2463 (1998).
[79]B. Cockburn and C. W. Shu, "The Runge–Kutta discontinuous Galerkin method for conservation laws V: Multidimensional systems," J. Comput. Phys. **141**, 199 (1998).
[80]P. L. Roe, "Approximate Riemann solvers, parameter vectors and difference schemes," J. Comput. Phys. **43**, 357–372 (1981).
[81]A. Marquina and P. Mulet, "A flux-split algorithm applied to conservative models for multicomponent compressible flows," J. Comput. Phys. **185**, 120–138 (2003).
[82]N. N. Smirnov, V. B. Betelin, R. M. Shagaliev, V. F. Nikitin, I. M. Belyakov, Y. N. Deryuguin, S. V. Aksenov, and D. A. Korchazhkin, "Hydrogen fuel rocket engines simulation using LOGOS code," Int. J. Hydrogen Energy **39**, 10748–10756 (2014).
[83]N. N. Smirnov, V. B. Betelin, V. F. Nikitin, L. I. Stamov, and D. I. Altoukhov, "Accumulation of errors in numerical simulations of chemically reacting gas dynamics," Acta Astronaut. **117**, 338–355 (2015).
[84]J. Ding, T. Si, M. Chen, Z. Zhai, X. Lu, and X. Luo, "On the interaction of a planar shock with a three-dimensional light gas cylinder," J. Fluid Mech. **828**, 289 (2017).
[85]L. Onsager, "Reciprocal relations in irreversible processes," Phys. Rev. **37**, 405 (1931).